Multiple time scales and pressure forcing in discontinuous Galerkin approximations to layered ocean models

Robert L. Higdon

Department of Mathematics
Oregon State University
Corvallis, Oregon 97331-4605

Abstract

This paper addresses some issues involving the application of discontinuous Galerkin (DG) methods to ocean circulation models having a generalized vertical coordinate. These issues include the following. (1) Determine the pressure forcing at cell edges, where the dependent variables can be discontinuous. In principle, this could be accomplished by solving a Riemann problem for the full system, but some ideas related to barotropic-baroclinic time splitting can be used to reduce the Riemann problem to a much simpler system of lower dimension. Such splittings were originally developed in order to address the multiple time scales that are present in the system. (2) Adapt the general idea of barotropic-baroclinic splitting to a DG implementation. A significant step is enforcing consistency between the numerical solution of the layer equations and the numerical solution of the vertically-integrated barotropic equations. The method used here has the effect of introducing a type of time filtering into the forcing for the layer equations, which are solved with a long time step. (3) Test these ideas in a model problem involving geostrophic adjustment in a multi-layer fluid. In certain situations, the DG formulation can give significantly better results than those obtained with a standard finite difference formulation.

Keywords: ocean modeling; multi-layer ocean models; discontinuous Galerkin; barotropic-baroclinic splitting; geostrophic adjustment

1. Introduction

The purpose of this paper is to develop, analyze, and test some procedures for using discontinuous Galerkin (DG) methods in multi-layer models of ocean circulation.

Email address: `higdon@math.oregonstate.edu` (Robert L. Higdon)

This work is an extension of the work described by Higdon [14]. That paper developed an integral weak form of the lateral pressure forcing that is suitable for usage with a DG method and with a generalized vertical coordinate that includes level, terrain-fitted, isopycnic, and hybrid coordinates as special cases. (Such coordinates are surveyed, for example, in [9] and [13].) This formulation was then analyzed, implemented, and tested for the special case of a single-layer fluid of constant density, i.e., for the shallow water equations. That analysis included numerical dispersion relations, a stability analysis of time-stepping schemes, and comparisons of accuracy and efficiency with some traditional finite difference methods. It was also shown that this formulation of the pressure forcing is automatically well-balanced, in the sense that variable bottom topography does not produce spurious forcing; further comments on this point are given in Section 2.2.1 of the present paper.

The present work extends the preceding work to multi-layer modeling. In particular, the following issues are addressed here.

(i) The pressure forcing term developed in [14] includes an integral around the boundary of a fluid region defined by a coordinate layer in the vertical dimension and a grid cell in the horizontal dimensions. (See Figure 1 in the present paper.) At a cell edge this integral is problematic; the integrand involves the pressure, which is not well-defined at a cell edge due to discontinuities across the edge. In principle, the values of dependent variables at a cell edge could be specified by solving a Riemann problem for the whole system, but in a model with many layers this process could be highly complicated. Instead, it is shown here that a simpler approach can be obtained by using ideas related to barotropic-baroclinic time splitting, a widely-used technique for addressing the multiple time scales that are present in the system. In such a splitting, the fast and slow dynamics are separated into distinct subsystems that are solved by different numerical techniques, especially different time-stepping methods. Such a splitting can also aid the computation of pressure at cell edges by confining the Riemann problem to a relatively simple system of lower dimension. In particular, a Riemann problem for the vertically-integrated barotropic equations can be used to remove problems associated with a discontinuous free surface. Any remaining internal discontinuities can then be addressed with simple averaging.

(ii) The general process of barotropic-baroclinic time splitting is adapted here to the specific case of DG methods. During the implementation of such a splitting, one necessary step is to enforce consistency between the numerical solution of the vertically-integrated barotropic equations and the numerical solution of the layer equations. The layer equations are solved explicitly with long time steps, although they allow motions varying on both the fast time scale and the slow time scale. The method described here for enforcing consistency has the effect of introducing a kind of time filtering into the forcing terms for the layer equations, and this appears to be a mechanism that enables the layer equations to be solved with long time steps.

(iii) The methodology in (i) and (ii) is tested in a model problem involving the adjustment of a multi-layer fluid to a state of geostrophic balance. In this problem, a discontinuous initial state is not in a state of balance, and the bal-

anced state is reached via propagation of inertia-gravity waves away from the location of the initial imbalance. In general, the process of geostrophic adjustment is an important mechanism in the evolution of geophysical fluid flows. In the test problem considered here, a DG algorithm can give much better results than a code based on the staggered C-grid, which is one of the finite difference grids that is traditionally used in ocean modeling.

Discontinuous Galerkin methods have been used extensively to solve the two-dimensional shallow water equations for a single-layer fluid of constant density; examples of recent work include Bao et al. [2], Giraldo and Warburton [7], Kubatko et al. [17], and Wirasaet et al. [24]. In the area of three-dimensional flows, Kärnä et al. [15] developed a coastal DG model that uses a terrain-fitted vertical coordinate with a moving vertical mesh, and Aizinger and Dawson [1] developed a three-dimensional DG shallow water model with a level vertical coordinate. Applications of DG methods to atmospheric flows include the works of Nair et al. [20] and Kopera and Giraldo [16]. On the other hand, in the numerical modeling of the three-dimensional general circulation of the ocean, operational models tend to use finite difference and finite volume methods on logically-rectangular grids (e.g., Griffies [9]); a recent exception is the usage of such methods on variable-resolution Voronoi grids (Ringler et al. [22], Petersen et al. [21]).

An outline of the present paper is as follows. Section 2 states the governing equations that will be considered here, including weak forms that are suitable for usage with DG spatial discretizations. Sections 3 and 4 develop the process of barotropic-baroclinic time splitting in the context of such spatial discretizations. Section 5 addresses the problem of computing pressure at cell edges, and Section 6 describes the results of some numerical computations. A summary is given in Section 7. The Appendix develops the exact solutions of the multi-layer geostrophic adjustment problem that is studied in Section 6.

2. Governing equations

The paper by Higdon [11] includes a derivation of partial differential equations that describe the conservation of momentum, mass, and tracers in a hydrostatic fluid that is in motion relative to a rotating spheroid. In that derivation, the horizontal coordinates are arbitrary orthogonal curvilinear coordinates, and the vertical coordinate is a generalized coordinate in the sense described above. Horizontal curvilinear coordinates are also included in the derivations in the more recent paper [14].

However, in the present paper the horizontal coordinates are assumed to be Cartesian coordinates, for the sake of notational simplicity. As in [14], the generalized vertical coordinate is a quantity s that is a non-decreasing function of the elevation z, at each horizontal position and time. It is also assumed here that the vertical length scale is much smaller than the horizontal length scale, for the motions of interest, so that the hydrostatic assumption is satisfied for those motions.

2.1. Pointwise form

In the present setting, the equations for conservation of momentum and mass can be written in the form

$$\frac{\partial}{\partial t}\big[u(-p_s)\big] + A_u - f\big(v(-p_s)\big) = -(gz_s)\frac{\partial P}{\partial x} + g\frac{\partial \tau_u}{\partial s} \tag{1}$$

$$\frac{\partial}{\partial t}\big[v(-p_s)\big] + A_v + f\big(u(-p_s)\big) = -(gz_s)\frac{\partial P}{\partial y} + g\frac{\partial \tau_v}{\partial s} \tag{2}$$

$$\frac{\partial}{\partial t}\big(p_s\big) + \frac{\partial}{\partial x}\big(up_s\big) + \frac{\partial}{\partial y}\big(vp_s\big) + \frac{\partial}{\partial s}\big(\dot{s}p_s\big) = 0. \tag{3}$$

Here, $u(x, y, s, t)$ and $v(x, y, s, t)$ are the x- and y-components of fluid velocity, respectively; f is the Coriolis parameter; $p(x, y, s, t)$ is the pressure; $P(x, y, z, t)$ is the pressure in terms of vertical coordinate z (discussed below, in Section 2.2.1); $z_s = \partial z/\partial s$, where $z(x, y, s, t)$ is the elevation corresponding to vertical coordinate s at horizontal position (x, y) and time t; $\dot{s} = Ds/Dt$ denotes the time derivative of s following fluid parcels; τ_u and τ_v are components of horizontal stress due to wind forcing and/or internal and bottom friction;

$$A_u = \frac{\partial}{\partial x}\Big[u\big(u(-p_s)\big)\Big] + \frac{\partial}{\partial y}\Big[v\big(u(-p_s)\big)\Big] + \frac{\partial}{\partial s}\Big[\dot{s}\big(u(-p_s)\big)\Big];$$

and A_v is obtained from A_u by replacing $u(-p_s)$ with $v(-p_s)$.

In the system (1)–(3) the quantity $-p_s = -\partial p/\partial s \geq 0$ serves as a mass density, and the quantities $u(-p_s)$ and $u(-p_s)$ are components of momentum density. In the special case where s is the elevation z, $-p_s = -p_z = \rho g$, where ρ is the density of the fluid and g is the (constant) magnitude of the acceleration due to gravity; and also $\dot{s} = \dot{z} = w$, which is the vertical component of fluid velocity. In this case, the system (1)–(3) reduces to a familiar form. Horizontal viscosity terms could be included in the momentum equations (1)–(2), but those effects will not be considered in the present discussion.

2.2. Spatial discretization and integral weak forms

Next we state integral weak forms of the momentum and mass equations, which are needed for implementation of discontinuous Galerkin methods. These forms are derived in [14] and are summarized here for the sake of usage in later sections.

In order to limit the complexity of the following discussions, assume from now on that all quantities in the system (1)–(3) are independent of y. In the numerical computations described in Section 6, this situation is realized by assuming flow in an infinite straight channel that is aligned with the y-direction. In the present framework, both of the velocity components u and v can be nonzero, but they depend on (x, s, t) instead of (x, y, s, t). It is also assumed here that the Coriolis parameter f is nonzero and constant.

In addition, it is assumed here that $\dot{s} = Ds/Dt = 0$. This assumption implies that the vertical advection terms need not be carried through the calculations, but it does not affect the structures of the remaining terms.

Partition the fluid domain vertically with coordinate surfaces of the form $s = s_r$ for $0 \leq r \leq L$, where s_0 refers to the top of the fluid, s_L refers to the bottom, and $s_0 > s_1 > \ldots > s_L$. Number the resulting layers from top to bottom. In terms of the vertical coordinate s, layer r is characterized by $s_r < s < s_{r-1}$; in terms of the elevation z, layer r is characterized by $z_r(x,t) < z < z_{r-1}(x,t)$, where $z_r(x,t) = z(x, s_r, t)$ and $z_{r-1}(x,t) = z(x, s_{r-1}, t)$ are the elevations of the bottom and top of the layer, respectively. Also partition the horizontal spatial interval with grid cells of the form $D_j = [x_{j-1/2}, x_{j+1/2}]$. These discretizations are illustrated in Figure 1.
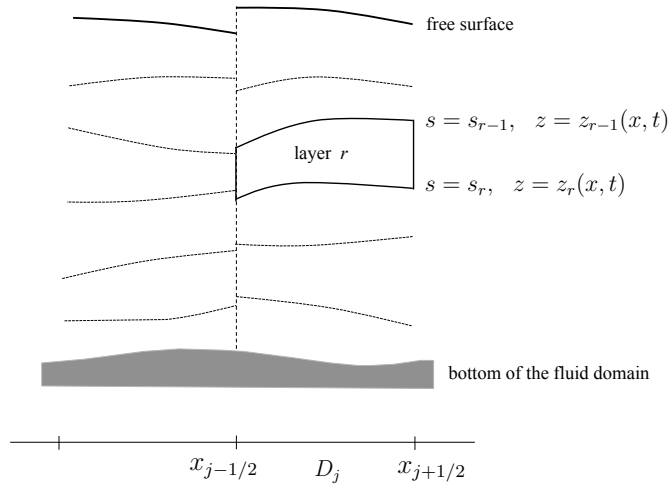

Figure 1: Horizontal and vertical discretizations of the fluid domain, as viewed from the side. The vertical coordinate in this figure is the elevation z. The curves show the locations of the free surface and the interfaces between layers. The figure allows for the possibility that these surfaces may be discontinuous at cell edges, in the case of a DG horizontal discretization and an arbitrary vertical coordinate. The weak forms stated here employ integration on the volume of fluid associated with grid cell D_j in the horizontal and layer r in the vertical.

The dependent variables that are encountered in the weak forms are the following. Vertical integration of the continuous mass variable $-p_s$ over layer r yields

$$\int_{s_r}^{s_{r-1}} (-p_s)\, ds = p(x, s_r, t) - p(x, s_{r-1}, t) \equiv \Delta p_r(x,t); \tag{4}$$

this quantity is the vertical pressure increment over layer r, and it is g times the mass per unit horizontal area in that layer. Now let

$$u_r(x,t) = \frac{1}{\Delta p_r} \int_{s_r}^{s_{r-1}} u(-p_s)\, ds \tag{5}$$

denote the mass-weighted vertical average of u in layer r; the vertically-integrated x-component of momentum is then $u_r \Delta p_r$. Similarly, the y-component is $v_r \Delta p_r$.

2.2.1. Weak form of the u-component of the momentum equation

The weak form of the u-component of the momentum equation, obtained by integration over grid cell D_j in the horizontal and layer r in the vertical, is (from [14])

$$\int_{D_j} \left\{ \frac{\partial}{\partial t} (u_r \Delta p_r) - f v_r \Delta p_r \right\} \psi(x) \, dx \; + \; \Phi_u(j, r, \psi)$$
$$= \; \Pi_u(j, r, \psi) \; + \; S_u(j, r, \psi), \tag{6}$$

where ψ is an arbitrary smooth test function. Here,

$$\Phi_u(j, r, \psi) = \left[u_r (u_r \Delta p_r) \psi(x) \right]_{x=x_{j-1/2}}^{x=x_{j+1/2}} \; - \int_{D_j} u_r (u_r \Delta p_r) \psi'(x) \, dx \tag{7}$$

arises from momentum fluxes, and

$$S_u(j, r, \psi) = g \int_{D_j} \left\{ (\tau_u)_{r-1}(x, t) - (\tau_u)_r(x, t) \right\} \psi(x) \, dx \tag{8}$$

represents shear stresses.

The quantity $\Pi_u(j, r, \psi)$ in equation (6) is the weak form of the pressure term, which is given by

$$\Pi_u(j, r, \psi) \;\; = \;\; - \left[H_r(x, t) \, \psi(x) \right]_{x=x_{j-1/2}}^{x=x_{j+1/2}} \; + \; \int_{D_j} H_r(x, t) \, \psi'(x) \, dx$$
$$+ \;\; g \int_{D_j} \left\{ p_{r-1}(x, t) \frac{\partial z_{r-1}}{\partial x} \; - \; p_r(x, t) \frac{\partial z_r}{\partial x} \right\} \psi(x) \, dx. \tag{9}$$

In equation (9), $p_{r-1}(x, t)$ and $p_r(x, t)$ denote the pressures at the top and bottom of layer r, i.e., $p_r(x, t) = p(x, s_r, t) = P(x, z_r(x, t), t)$. Also,

$$H_r(x, t) \;\; = \;\; g \int_{z_r(x,t)}^{z_{r-1}(x,t)} P(x, z, t) \, dz \tag{10}$$

$$= \;\; \int_{p_{r-1}(x,t)}^{p_r(x,t)} \alpha \, p \, dp \tag{11}$$

is the vertical integral of the horizontal pressure force, where $\alpha = 1/\rho$ is the specific volume (volume per unit mass). The derivation of (11) from (10) uses the hydrostatic condition $\partial P / \partial z = -\rho g = -g / \alpha$.

The quantities $\partial P / \partial x$ and $\partial P / \partial y$ on the right sides of the momentum equations (1) and (2) are partial derivatives for fixed z, evaluated at the point $(x, y, z(x, y, s, t), t)$. However, z need not be the vertical coordinate s that is used in the model, and relating these partial derivatives to functions of (x, y, s, t) leads to difficulties that are described in Section 2.4 of [14]. Instead of making such a conversion, the derivation of equation (6) in reference [14] is based on

6

proceeding directly to the weak form from the pointwise form (1), via integration on the region of fluid consisting of the portion of layer r that lies on the horizontal spatial interval D_j.

As suggested by Figure 1, the pressure may be discontinuous across cell edges, and this leads to an ambiguity in the value of the vertically-integrated pressure $H_r(x, t)$ when x is located on such an edge. This issue is addressed in Section 5.

In the case of the single-layer shallow water equations for a hydrostatic fluid of constant density, the region of integration used to obtain the weak form is the entire water column sitting on cell D_j. In Section 5.4 of [14] it is shown that the pressure forcing is automatically well-balanced, in the sense that variable bottom topography does not produce spurious forcing. That analysis assumed a particular representation of the pressure at cell edges; however, that assumption can be relaxed to require only that the algorithm for computing pressures at cell edges produces the continuous values when the free surface is continuous.

2.2.2. Weak forms of the mass and v-momentum equations

The integral weak form of the v-component of the momentum equation is

$$\int_{D_j} \left\{ \frac{\partial}{\partial t} (v_r \Delta p_r) + f u_r \Delta p_r \right\} \psi(x) \ dx \ + \ \Phi_v(j, r, \psi) \ = \ S_v(j, r, \psi), \quad (12)$$

where $\Phi_v(j, r, \psi)$ and $S_v(j, r, \psi)$ are analogues of (7) and (8), respectively. A pressure term is not present in this equation because all quantities are assumed to be independent of y. The weak form of the mass equation is

$$\int_{D_j} \frac{\partial}{\partial t} (\Delta p_r) \psi(x) \ dx \ + \ \Phi_p(j, r, \psi) \ = \ 0, \quad (13)$$

where

$$\Phi_p(j, r, \psi) = \left[u_r (\Delta p_r) \psi(x) \right]_{x=x_{j-1/2}}^{x=x_{j+1/2}} - \int_{D_j} u_r (\Delta p_r) \psi'(x) \ dx. \quad (14)$$

3. Barotropic equations

In the numerical modeling of ocean circulation it is a widespread practice to split the fast and slow dynamics into separate subsystems that are solved by different techniques. General reviews of this process are given, for example, by Griffies [9] and Higdon [11]. The splitting process is motivated by the idea of external and internal modes, which can be developed analytically in idealized cases of linearized flow. Derivations of these modes for the vertically-continuous case are included in [11] and in the text by Gill [6], and some special cases for the vertically-discrete case are developed in the Appendix of the present paper. These ideas are illustrated in the analysis in Section 5 and in the description of numerical computations in Section 6.

In the case of a pure external motion, all fluid layers are thickened or thinned by approximately the same proportion, at each horizontal location and time, and the horizontal fluid velocity is approximately independent of vertical position. Knowledge of the free surface elevation and the horizontal velocity at the top of the fluid thus reveals (approximately) the mass and velocity fields throughout the interior. This suggests that external motions might be modeled by a simpler two-dimensional system instead of a fully three-dimensional system. On the other hand, internal motions are manifested by undulations of density surfaces within the fluid, the free surface remains nearly level, and the mass-weighted vertical average of horizontal velocity is nearly zero. In the case of gravity wave motions, the restoring force in the external mode is due to the density contrast between water and air, whereas the restoring force in the internal modes is due to density contrasts within the fluid and is thus much weaker and generates much slower motions.

The dynamics of these modes suggest that the fast external motions can be modeled by a vertically-integrated system that resembles the shallow water equations for a fluid of constant density; in fact, in the linearized case, vertical summations approximate projections onto the external mode. (See [11].) The slower internal and advective motions can be modeled by a more complicated system that is fully three-dimensional. The fast and slow systems are often referred to as the "barotropic" equations and "baroclinic" equations, respectively. The fast barotropic equations can be solved either explicitly with a relatively short time step or implicitly with a relatively long time step, whereas the slow baroclinic equations are solved explicitly with a long time step.

In the present section we derive the integral weak forms of the barotropic equations that correspond to the governing equations stated in Section 2.2. The pointwise forms of these equations are also stated here. In the following section we describe a numerical implementation of a barotropic-baroclinic splitting based on those equations and on discontinuous Galerkin spatial discretizations.

For the vertically-integrated versions of the integral weak forms stated in Section 2.2, the dependent variables are the following. Let

$$p_b(x,t) = \sum_{r=1}^{L} \Delta p_r(x,t) = \int_{s_L}^{s_0} -p_s(x,s,t)\,ds. \tag{15}$$

(See (4).) This quantity is g times the mass per unit horizontal area in the entire water column, and it will serve as the barotropic mass variable. Also let

$$\bar{u}(x,t) = \sum_{r=1}^{L} \frac{\Delta p_r(x,t)}{p_b(x,t)} u_r(x,t) = \frac{1}{p_b(x,t)} \int_{s_L}^{s_0} u(x,s,t)(-p_s(x,s,t))\,ds \tag{16}$$

(see (5)) denote the mass-weighted vertical average of u over the water column; this quantity is the u-component of barotropic velocity. The u-component of barotropic momentum density (times g) is then

$$p_b\bar{u} = \sum_{r=1}^{L} u_r(x,t)\Delta p_r(x,t). \tag{17}$$

8

The v-component of barotropic momentum is $p_b\bar{v}$, where $\bar{v}$ is defined in analogy to (16).

It will also be useful to refer to the baroclinic velocity, for which the u-component is $u'_r(x,t) = u_r(x,t) - \bar{u}(x,t)$ for $1 \le r \le L$. The total velocity then has the decomposition

$$u_r(x,t) = \bar{u}(x,t) + u'_r(x,t), \tag{18}$$

and a comparison to (15) and (16) shows

$$\sum_{r=1}^{L} \frac{\Delta p_r(x,t)}{p_b(x,t)} u'_r(x,t) = \sum_{r=1}^{L} \frac{\Delta p_r}{p_b} u_r - \sum_{r=1}^{L} \frac{\Delta p_r}{p_b} \bar{u} = \bar{u} - \bar{u} = 0. \tag{19}$$

The baroclinic velocity u'_r thus has mass-weighted vertical average equal to zero. The v-component v'_r can be defined similarly.

3.1. Weak form of the barotropic u-momentum equation

To obtain the weak form of the barotropic u-momentum equation, sum the layer momentum equation (6) over all layers (i.e., for $1 \le r \le L$) to obtain

$$\int_{D_j} \left\{ \frac{\partial}{\partial t} (p_b\bar{u}) - fp_b\bar{v} \right\} \psi(x)\ dx\ +\ \overline{\Phi_u}(j,\psi)$$
$$=\ \overline{\Pi_u}(j,\psi)\ +\ \overline{S_u}(j,\psi). \tag{20}$$

The momentum variables $p_b\bar{u}$ and $p_b\bar{v}$ are obtained by reference to (17) and its analogue for the v-component, and the terms $\overline{\Phi_u}(j,\psi)$, $\overline{\Pi_u}(j,\psi)$, and $\overline{S_u}(j,\psi)$ are vertical sums of corresponding terms in (6).

The advection term $\overline{\Phi_u}(j,\psi)$ can be written as

$$\overline{\Phi_u}(j,\psi)\ =\ \sum_{r=1}^{L} \Phi_u(j,r,\psi)$$
$$=\ \Big[Q_u(x,t)\psi(x)\Big]_{x=x_{j-1/2}}^{x=x_{j+1/2}}\ -\ \int_{D_j} Q_u(x,t)\psi'(x)\ dx, \tag{21}$$

where

$$Q_u(x,t)\ =\ \sum_{r=1}^{L} u_r(u_r\Delta p_r) = \sum_{r=1}^{L} (\bar{u} + u'_r)(\bar{u} + u'_r)\Delta p_r$$
$$=\ \bar{u}(p_b\bar{u}) + p_b \left(\sum_{r=1}^{L} u'_r u'_r \frac{\Delta p_r}{p_b} \right). \tag{22}$$

The last equality in (22) uses the definition of p_b in (15) and the statement (19) that the mass-weighted vertical average of u'_r is zero. The quantity Q_u serves as a flux of barotropic momentum.

The barotropic stress term $\overline{S_u}(j, \psi)$ is a telescoping sum that reduces to

$$\overline{S_u}(j, \psi) = g \int_{D_j} \left\{ (\tau_u)_{top}(x, t) - (\tau_u)_{bot}(x, t) \right\} \psi(x) \ dx. \tag{23}$$

Here, the subscripts *top* and *bot* refer to the top and bottom of the fluid domain.

The barotropic pressure term $\overline{\Pi_u}(j, \psi)$ is

$$
\begin{aligned}
\overline{\Pi_u}(j, \psi) &= \sum_{r=1}^{L} \Pi_u(j, r, \psi) \\
&= -\left[H(x, t) \ \psi(x) \right]_{x=x_{j-1/2}}^{x=x_{j+1/2}} + \int_{D_j} H(x, t) \ \psi'(x) \ dx \tag{24} \\
&+ g \int_{D_j} \left\{ p_{top}(x, t) \frac{\partial z_{top}}{\partial x} - p_{bot}(x, t) \frac{\partial z_{bot}}{\partial x} \right\} \psi(x) \ dx.
\end{aligned}
$$

where

$$
\begin{aligned}
H(x, t) &= \sum_{r=1}^{L} H_r(x, t) \\
&= g \int_{z_{bot}(x,t)}^{z_{top}(x,t)} P(x, z, t) \ dz = \int_{p_{top}(x,t)}^{p_{bot}(x,t)} \alpha \, p \ dp. \tag{25}
\end{aligned}
$$

(See (10) and (11).)

3.2. Weak forms of the barotropic mass and v-momentum equations

The integral weak form of the barotropic v-momentum equation is

$$\int_{D_j} \left\{ \frac{\partial}{\partial t} (p_b \bar{v}) + f p_b \bar{u} \right\} \psi(x) \ dx + \overline{\Phi_v}(j, \psi) = \overline{S_v}(j, \psi), \tag{26}$$

where $\overline{S_v}(j, \psi)$ is an analogue of $\overline{S_u}(j, \psi)$ in (23), and

$$\overline{\Phi_v}(j, \psi) = \left[Q_v(x, t) \psi(x) \right]_{x=x_{j-1/2}}^{x=x_{j+1/2}} - \int_{D_j} Q_v(x, t) \psi'(x) \ dx, \tag{27}$$

with

$$Q_v(x, t) = \bar{u}(p_b \bar{v}) + p_b \left(\sum_{r=1}^{L} u_r' v_r' \frac{\Delta p_r}{p_b} \right). \tag{28}$$

The weak form of the barotropic mass equation is a vertical sum of (13) and is given by

$$\int_{D_j} \frac{\partial p_b}{\partial t} \psi(x) \ dx + \overline{\Phi_p}(j, \psi) = 0, \tag{29}$$

where

$$\overline{\Phi_p}(j, \psi) = \left[(p_b \bar{u}) \psi(x) \right]_{x=x_{j-1/2}}^{x=x_{j+1/2}} - \int_{D_j} (p_b \bar{u}) \psi'(x) \ dx. \tag{30}$$

The quantity $p_b \bar{u}$ is the barotropic mass flux (times g).

10

For the sake of clarity, it may be useful to note the pointwise forms of the barotropic equations. Each of the weak forms (20), (26), and (29) includes terms that have the appearance of integration by parts. For each such equation, un-do the integration by parts and use the fact that the test function ψ is arbitrary to obtain the system

$$
\begin{aligned}
\frac{\partial}{\partial t}\left(p_b \bar{u}\right) + \frac{\partial Q_u}{\partial x} - f p_b \bar{v} &= -\frac{\partial H}{\partial x} + g\left[p_{top}(x,t)\frac{\partial z_{top}}{\partial x} - p_{bot}(x,t)\frac{\partial z_{bot}}{\partial x}\right] \\
&\quad + g\left[(\tau_u)_{top}(x,t) - (\tau_u)_{bot}(x,t)\right] \\
\frac{\partial}{\partial t}\left(p_b \bar{v}\right) + \frac{\partial Q_v}{\partial x} + f p_b \bar{u} &= g\left[(\tau_v)_{top}(x,t) - (\tau_v)_{bot}(x,t)\right] \\
\frac{\partial p_b}{\partial t} + \frac{\partial}{\partial x}\left(p_b \bar{u}\right) &= 0.
\end{aligned}
\tag{31}
$$

An alternate approach to deriving the weak forms of the barotropic equations is to begin by integrating the continuous equations vertically over each layer to obtain equations that are pointwise in horizontal position and time (as in Section 3.3 of [14]), then sum vertically to obtain (31), and finally multiply by a test function and integrate.

The vertically-integrated equations (31) are similar to the shallow water equations for a single-layer hydrostatic fluid of constant density. In addition, for the case of general ocean circulation the dynamics of the barotropic equations are nearly linear, in the sense that the velocity components $\bar{u}$ and $\bar{v}$ have maximum magnitudes on the order of at most one percent of the speed of external gravity waves, and the relative variation of p_b is typically much less than one percent.

4. Numerical implementation of barotropic-baroclinic splitting

The present section describes a numerical implementation of a barotropic-baroclinic splitting of the governing equations stated in Section 2.2, with DG spatial discretizations.

In the following, the term "layer equations" refers to the system (6), (12), and (13), which models the momentum and mass in each layer in the fluid. A significant issue in this discussion is enforcing consistency between the numerical solution of the layer equations and the numerical solution of the vertically-integrated barotropic equations. The procedures described here for enforcing consistency have the effect of introducing a kind of time filtering into the forcing for the layer equations, and the resulting filtered equations will be regarded as the slow "baroclinic" equations.

4.1. Discontinuous Galerkin space discretization

In a DG representation of the solution, each dependent variable in each grid cell is represented as a polynomial in x with coefficients that depend on t. Here,

we derive a system of ordinary differential equations for the time-dependent degrees of freedom in those polynomials.

For any positive integer M, let $\mathcal{P}^M(D_j)$ denote the space of polynomials of degree M or less on cell D_j. Also, for any integer $m \geq 0$ let P_m be the Legendre polynomial of degree m on the reference interval $[-1, 1]$, with P_m normalized so that $P_m(1) = 1$. These polynomials satisfy the orthogonality condition $\int_{-1}^1 P_m P_n = 2/(2m+1)$ if $m = n$ and $\int_{-1}^1 P_m P_n = 0$ otherwise. Now let

$$\psi_m^{(j)}(x) = P_m\left(\frac{2}{\Delta x}(x - x_j)\right) \tag{32}$$

for $x_{j-1/2} < x < x_{j+1/2}$ and $0 \leq m \leq M$. Here, x_j is the center of cell $D_j = [x_{j-1/2}, x_{j+1/2}]$, and $\Delta x = x_{j+1/2} - x_{j-1/2}$. (For notational simplicity, any dependence of the grid size Δx on the index j is suppressed from the notation.) The set $\left\{\psi_0^{(j)}, \psi_1^{(j)}, \ldots, \psi_M^{(j)}\right\}$ is a (modal) basis of the space $\mathcal{P}^M(D_j)$, with the orthogonality relations

$$\int_{D_j} \psi_m^{(j)} \psi_n^{(j)} = \begin{cases} \frac{\Delta x}{2m+1} & \text{if } m = n \\ 0 & \text{if } m \neq n. \end{cases} \tag{33}$$

The dependent variables in the layer equations (6), (12), and (13) can be represented as

$$(u_r \Delta p_r)(x, t) = \sum_{n=0}^{M} U_{r,n}^{(j)}(t) \, \psi_n^{(j)}(x)$$

$$(v_r \Delta p_r)(x, t) = \sum_{n=0}^{M} V_{r,n}^{(j)}(t) \, \psi_n^{(j)}(x) \tag{34}$$

$$(\Delta p_r)(x, t) = \sum_{n=0}^{M} \delta_{r,n}^{(j)}(t) \, \psi_n^{(j)}(x)$$

for all $x \in D_j$, all t, and $1 \leq r \leq L$. (With an abuse of notation, the approximations to $u_r \Delta p_r$, $v_r \Delta p_r$, and Δp_r are also denoted by $u_r \Delta p_r$, $v_r \Delta p_r$, and Δp_r.) The coefficients $U_{r,n}^{(j)}(t)$, $V_{r,n}^{(j)}(t)$, and $\delta_{r,n}^{(j)}(t)$ will be regarded as "degrees of freedom" for the corresponding momentum and mass variables.

To obtain a DG discretization of equation (6), the u-component of the momentum equation in layer r, insert the representations of $u_r \Delta p_r$ and $v_r \Delta p_r$ in (34) into the left side of (6) and require that this equation hold for all $\psi \in \mathcal{P}^M(D_j)$. Equivalently, this equation should hold for $\psi = \psi_m^{(j)}$ for $0 \leq m \leq M$. The orthogonality condition (33) then yields

$$\frac{dU_{r,m}^{(j)}}{dt} = fV_{r,m}^{(j)}(t)$$

$$+ \frac{2m+1}{\Delta x}\left[-\Phi_u(j, r, \psi_m^{(j)}) + \Pi_u(j, r, \psi_m^{(j)}) + S_u(j, r, \psi_m^{(j)})\right] \tag{35}$$

12

for $0 \leq m \leq M$, all layers r with $1 \leq r \leq L$, and all grid cells D_j. The quantities $\Phi_u(j, r, \psi_m^{(j)})$, $\Pi_u(j, r, \psi_m^{(j)})$, and $S_u(j, r, \psi_m^{(j)})$ are obtained from (7), (8), and (9), and they involve integrals of dependent variables and other derived quantities on the cell D_j and also the pointwise values of various quantities at the edges of D_j. In practice, with an explicit time-stepping method the quantities Φ_u, Π_u, and S_u can be computed from pointwise evaluations and numerical quadrature schemes. For reasons of complexity, only explicit time-stepping methods will be considered in the present paper, both for the layer equations and for the barotropic equations.

The DG discretization of the v-momentum equation (12) in layer r is

$$
\begin{aligned}
\frac{dV_{r,m}^{(j)}}{dt} &= -fU_{r,m}^{(j)}(t) \\
&+ \frac{2m+1}{\Delta x}\left[-\Phi_v(j, r, \psi_m^{(j)}) + S_v(j, r, \psi_m^{(j)})\right]
\end{aligned}
\tag{36}
$$

for $0 \leq m \leq M$, $1 \leq r \leq L$, and all j. The DG discretization of the layer mass equation (13) is

$$
\frac{d\delta_{r,m}^{(j)}}{dt} = -\left(\frac{2m+1}{\Delta x}\right)\Phi_p(j, r, \psi_m^{(j)}),
\tag{37}
$$

where $\Phi_p(j, r, \psi_m^{(j)})$ is obtained from (14).

Discontinuous Galerkin discretizations of the barotropic equations can be obtained in a similar manner. The dependent variables in the barotropic equations (20), (26), and (29) can be represented as

$$
\begin{aligned}
(p_b\bar{u})(x, t) &= \sum_{n=0}^{M} \overline{U_n^{(j)}}(t)\,\psi_n^{(j)}(x) \\
(p_b\bar{v})(x, t) &= \sum_{n=0}^{M} \overline{V_n^{(j)}}(t)\,\psi_n^{(j)}(x) \\
p_b(x, t) &= \sum_{n=0}^{M} \overline{\delta_n^{(j)}}(t)\,\psi_n^{(j)}(x)
\end{aligned}
\tag{38}
$$

for all $x \in D_j$ and all t. Calculations similar to the preceding yield

$$
\begin{aligned}
\frac{d\overline{U_m^{(j)}}}{dt} &= f\overline{V_m^{(j)}}(t) \\
&+ \frac{2m+1}{\Delta x}\left[-\overline{\Phi_u}(j, \psi_m^{(j)}) + \overline{\Pi_u}(j, \psi_m^{(j)}) + \overline{S_u}(j, \psi_m^{(j)})\right]
\end{aligned}
\tag{39}
$$

$$
\begin{aligned}
\frac{d\overline{V_m^{(j)}}}{dt} &= -f\overline{U_m^{(j)}}(t) \\
&+ \frac{2m+1}{\Delta x}\left[-\overline{\Phi_v}(j, \psi_m^{(j)}) + \overline{S_v}(j, \psi_m^{(j)})\right]
\end{aligned}
\tag{40}
$$

$$
\frac{d\overline{\delta_m^{(j)}}}{dt} = -\left(\frac{2m+1}{\Delta x}\right)\overline{\Phi_p}(j, \psi_m^{(j)})
\tag{41}
$$

13

for $0 \leq m \leq M$ and all cells D_j.

4.2. Consistency between the layer equations and the barotropic equations

A numerical implementation of a barotropic-baroclinic splitting, for the systems considered here, can be based on solving the fast barotropic equations with a short time step and solving the layer equations explicitly with a long time step that is appropriate for representing the slow motions in the system. However, this approach encounters two difficulties.

(i) The vertical sums of the momentum and mass variables computed with the layer equations need not equal exactly the computed values of the corresponding barotropic variables, even though the barotropic equations are derived by summing the layer equations vertically. This discrepancy is due to different numerical discretizations being used for the two systems, and the discrepancy is at the level of truncation error.

(ii) In general, the layer equations can admit both fast and slow motions, and the long time step used for those equations could lead to numerical instability.

Some procedures developed in this subsection will address both of these difficulties simultaneously. These procedures are related to some methods developed by Higdon [10], [12] (and in unpublished work by others mentioned in [10] and [12]) for the case of finite difference and finite volume methods. In both the DG and finite difference/volume cases, the main idea is to produce the desired consistency by introducing suitable (small) adjustments to the forcing terms in the layer equations. These adjustments also yield a type of time filtering that addresses difficulty (ii) stated above. In the case of finite difference/volume methods, the adjustments are applied directly to the pointwise values of the dependent variables that are computed with such methods. On the other hand, in the case of DG methods the adjustments are applied to the degrees of freedom for those variables. Due to the different nature of the setting considered here, the procedures for the present case are described in some detail.

4.2.1. An algorithm for obtaining consistency in the mass equations

Here we address the consistency between the barotropic mass and the masses in the layers.

Let t_n and $t_{n+1} = t_n + \Delta t$ denote consecutive time levels for which the layer equations are solved, and assume that the fast barotropic equations are solved with time step $\Delta t/N$, where N denotes the number of barotropic subintervals of the baroclinic time interval $[t_n, t_{n+1}]$. Denote the approximation to the layer mass $(\Delta p_r)(x, t_{n+1})$ by

$$(\Delta p_r)^{n+1}(x) = \sum_{m=0}^{M} \left(\delta_{r,m}^{(j)} \right)^{n+1} \psi_m^{(j)}(x)$$

for all $x \in D_j$, and denote the approximation to the barotropic mass $p_b(x, t_{n+1})$ by

$$p_b^{n+1}(x) = \sum_{m=0}^{M} \left(\overline{\delta_m^{(j)}} \right)^{n+1} \psi_m^{(j)}(x).$$

The consistency condition

$$\sum_{r=1}^{L} (\Delta p_r)^{n+1}(x) = p_b^{n+1}(x)$$

is equivalent to

$$\sum_{r=1}^{L} \left(\delta_{r,m}^{(j)}\right)^{n+1} = \left(\overline{\delta_m^{(j)}}\right)^{n+1} \tag{42}$$

for $0 \leq m \leq M$, since the functions $\psi_0^{(j)}$, $\psi_1^{(j)}$, ..., $\psi_M^{(j)}$ are linearly independent on cell D_j. That is, the consistency condition can be enforced mode-by-mode. Statements analogous to (42) can be made for the components of momentum.

Equation (37) for mode m of the layer mass can be discretized with a time-stepping method of the form

$$\left(\delta_{r,m}^{(j)}\right)^{*} = \left(\delta_{r,m}^{(j)}\right)^{n} - (2m+1)\frac{\Delta t}{\Delta x} \left(A_{r,m}^{(j)}\right)^{n+1}, \tag{43}$$

where

$$\left(A_{r,m}^{(j)}\right)^{n+1} = \left[F_r^{n+1}(x)\psi_m^{(j)}(x)\right]_{x=x_{j-1/2}}^{x=x_{j+1/2}} - \int_{D_j} F_r^{n+1}(x)\frac{d\psi_m^{(j)}}{dx}\ dx.$$

Here, the quantity $\Phi_p(j, r, \psi_m^{(j)})$ in (37) is obtained from (14), and $F_r^{n+1}(x)$ is a discretization of the layer mass flux $u_r \Delta p_r$. Values of $F_r^{n+1}(x)$ at cell edges are obtained from a mass flux algorithm (e.g., upwind), and values of $F_r^{n+1}(x)$ in the interior of cell D_j are obtained from the degrees of freedom for dependent variables. The quantities used to compute $F_r^{n+1}(x)$ are not necessarily evaluated at time t_{n+1}; instead, the superscript $n+1$ simply indicates that these quantities are used to obtain the solution at time t_{n+1}.

The quantity $\left(\delta_{r,m}^{(j)}\right)^{*}$ on the left side of (43) would be the numerical solution at time t_{n+1}, except for the need to enforce the consistency condition (42). The condition (42) will be enforced with the modified method

$$\left(\delta_{r,m}^{(j)}\right)^{n+1} = \left(\delta_{r,m}^{(j)}\right)^{n} - (2m+1)\frac{\Delta t}{\Delta x} \left(B_{r,m}^{(j)}\right)^{n+1}, \tag{44}$$

where

$$\left(B_{r,m}^{(j)}\right)^{n+1} = \left[\left(F_r^{n+1}(x) + w_r^{(j)}C^{(j)}(x)\right)\psi_m^{(j)}(x)\right]_{x=x_{j-1/2}}^{x=x_{j+1/2}}$$

$$- \int_{D_j} \left(F_r^{n+1}(x) + w_r^{(j)}C^{(j)}(x)\right)\frac{d\psi_m^{(j)}}{dx}\ dx. \tag{45}$$

The quantity $C^{(j)}$ is a flux adjustment, and $w_1^{(j)}$, ..., $w_L^{(j)}$ are nonnegative weight coefficients with sum 1 which are used to distribute the flux adjustment to the various layers. These quantities are specified below.

15

Now assume that equation (41) for mode m of the barotropic mass is discretized with time step $\Delta t / N$ and an equation of the form

$$\left(\overline{\delta_m^{(j)}}\right)^{n,i+1} = \left(\overline{\delta_m^{(j)}}\right)^{n,i} - \left(\frac{2m+1}{\Delta x}\right)\frac{\Delta t}{N}\left(\overline{A_m^{(j)}}\right)^{n,i+1} \tag{46}$$

for $0 \le i \le N-1$. The superscript "n, i" refers to barotropic substep i of the baroclinic time interval $[t_n, t_{n+1}]$, i.e.. to time $t_{n,i} = t_n + (i/N)\Delta t$, and

$$\left(\overline{A_m^{(j)}}\right)^{n,i+1} = \left[\overline{F^{n,i+1}}(x)\psi_m^{(j)}(x)\right]_{x=x_{j-1/2}}^{x=x_{j+1/2}} - \int_{D_j} \overline{F^{n,i+1}}(x)\frac{d\psi_m^{(j)}}{dx}\ dx. \tag{47}$$

Here, $\overline{F^{n,i+1}}$ is a discretization of the barotropic mass flux $p_b \bar{u}$ which is used to compute the solution at barotropic time step $t_{n,i+1}$. (Also see (30).) A relation between quantities defined on the barotropic and baroclinic time grids is given by

$$\left(\overline{\delta_m^{(j)}}\right)^{n,0} = \left(\overline{\delta_m^{(j)}}\right)^{n} \qquad \text{and} \qquad \left(\overline{\delta_m^{(j)}}\right)^{n,N} = \left(\overline{\delta_m^{(j)}}\right)^{n+1},$$

where single superscripts refer to baroclinic time levels.

The cumulative effect of the discretization (46) over all of the barotropic subintervals of the baroclinic time interval $[t_n, t_{n+1}]$ is obtained by summing (46) for $0 \le i \le N-1$ and canceling some terms to obtain

$$\left(\overline{\delta_m^{(j)}}\right)^{n+1} = \left(\overline{\delta_m^{(j)}}\right)^{n} - (2m+1)\frac{\Delta t}{\Delta x}\left[\frac{1}{N}\sum_{i=0}^{N-1}\left(\overline{A_m^{(j)}}\right)^{n,i+1}\right]. \tag{48}$$

On the other hand, the vertical sum (for $1 \le r \le L$) of the layer method (44) is

$$\sum_{r=1}^{L}\left(\delta_{r,m}^{(j)}\right)^{n+1} = \sum_{r=1}^{L}\left(\delta_{r,m}^{(j)}\right)^{n} - (2m+1)\frac{\Delta t}{\Delta x}\left[\sum_{r=1}^{L}\left(B_{r,m}^{(j)}\right)^{n+1}\right]. \tag{49}$$

A comparison of (48) and (49) shows that the consistency condition (42) is satisfied at time t_{n+1}, assuming that it is already satisfied at time t_n, if and only if

$$\sum_{r=1}^{L}\left(B_{r,m}^{(j)}\right)^{n+1} = \frac{1}{N}\sum_{i=0}^{N-1}\left(\overline{A_m^{(j)}}\right)^{n,i+1},$$

i.e., the vertical sum of the layer forcing equals the time average of the barotropic forcing. A sufficient condition for this to occur is

$$\sum_{r=1}^{L}\left(F_r^{n+1} + w_r^{(j)}C^{(j)}\right) = \frac{1}{N}\sum_{i=0}^{N-1}\overline{F^{n,i+1}}. \tag{50}$$

(See (45) and (47).) Since the weights have sum equal to 1, (50) holds if and only if

$$C^{(j)} = -\sum_{r=1}^{L}F_r^{n+1} + \frac{1}{N}\sum_{i=0}^{N-1}\overline{F^{n,i+1}}. \tag{51}$$

The quantity $C^{(j)}$ is then inserted into equation (45) in order to specify completely the method (44) for updating the masses in the layers.

16

4.2.2. Remarks on consistency of mass

Following are some remarks about preceding process of obtaining consistency.

(a) The first sum on the right side of (51) is the vertical sum of discretizations of the mass fluxes $u_r \Delta p_r$ in the layers, and the second term is a time average of discretizations of the barotropic mass flux $p_b \bar{u}$. As $\Delta x \to 0$ and $\Delta t \to 0$, these quantities approach the same limit, since $p_b \bar{u} = \sum_{r=1}^{L} u_r \Delta p_r$ in the continuous problem. The quantity $C^{(j)}$ in (51) is thus due entirely to truncation error, and its usage in (44) and (45) amounts to a manipulation of truncation error so as to achieve the desired goal of consistency between the barotropic mass equation and the mass equations in the layers.

(b) The quantity $C^{(j)}$ in (51) has units of mass flux (more precisely, g times mass flux, or pressure times velocity) and can therefore be written as $C^{(j)} = p_b u_a$, where u_a has units of velocity. The (small) velocity u_a is used to adjust the mass fluxes in the layers so that the vertical sum of the adjusted layer fluxes equals the time average of the barotropic flux.

(c) The weights $w_1^{(j)}$, ..., $w_L^{(j)}$ in (45) are used to distribute the flux correction $C^{(j)}$ over the various layers. In the code that was used to perform the computations described in Section 6, these weights are relative layer thicknesses, as measured by the cell averages of Δp_r and $p_b = \sum_{r=1}^{L} \Delta p_r$. To be more precise, the zero-order degrees of freedom in the representations (34) and (38) are cell averages, since the basis functions of positive degree have integral zero on cell D_j (due to orthogonality of Legendre polynomials). Assume that the cell averages $\left(\delta_{r,0}^{(j)} \right)^*$ obtained from (43) with $m = 0$ are nonnegative, for all layers r and all cells D_j. (In general, this may require a suitable usage of limiters, although this point will not be addressed in the present paper.) The weights used here are then given by

$$w_r^{(j)} = \frac{\left(\delta_{r,0}^{(j)} \right)^{n+1}}{\sum_{k=1}^{L} \left(\delta_{k,0}^{(j)} \right)^{n+1}} \tag{52}$$

for $1 \leq r \leq L$. These weights are computed at quadrature points in the cells and also at cell edges. In the case of cell edges, the quantities in (52) are chosen in an upwind fashion, where "upwind" is defined by the sign of the quantity $C^{(j)}$ in (51) (or, equivalently, by the sign of the adjustment velocity u_a discussed in remark (b) above). The application of the adjustment in (44) and (45) for the case $m = 0$ is then a simple upwind finite-volume step starting from data $\left(\delta_{r,0}^{(j)} \right)^*$, and the nonnegativity of cell averages is therefore preserved under the adjustment process.

4.2.3. Interpretation as time filtering of the forcing in the layer equations

The vertical sum in (51) can be regarded as the fast part of the flux in the mass equation in the layers, as this vertical summation approximates a

projection onto the external mode. (See the beginning of Section 3.) This part of the forcing is not resolved on a time grid with the relatively long time step Δt, which is used in the layer equations and is intended to resolve the slow motions in the system. On the other hand, the second term on the right side of (51) is a time average of well-resolved fluxes that are computed when the barotropic equations are solved with relatively short time steps. The usage of the flux correction $C^{(j)}$ from (51) in the layer method (44)–(45) amounts to subtracting layer r's share of the unresolved fast forcing from the layer equation and then replacing it with the time average of well-resolved forcing from the barotropic equation. In this sense, the method (44)–(45) can be regarded as a time-filtered method for which the long time step Δt can be used successfully, as in the numerical computations in Section 6.

The same interpretation can be given to the process of obtaining consistency in the momentum equations that is described below, in Section 4.2.4. In particular, the correction term (59) used in that section is a close analogue of the correction term (51) discussed above.

Analogous interpretations for the mass and momentum equations in the case of finite difference methods are given by Higdon [12].

4.2.4. Consistency in the momentum equations

Here we address the consistency between the barotropic u-component of momentum and the u-component of momentum in the layers. The v-component can be treated similarly.

In the case of the mass equations, consistency is obtained by an adjustment of the lateral mass fluxes in the layers. Adjustment of fluxes maintains the local conservation of mass in the numerical method, and it also enables the preservation of nonnegative cell averages of layer thickness, as noted in Remark (c) in Section 4.2.2. However, in the case of the momentum equations several processes are represented (momentum advection, Coriolis term, pressure, and stresses), and for the momentum variables it is less clear that an adjustment of fluxes would be suitable. Instead, a different approach will be used for the momentum equations.

Denote the approximations to the layer momentum $(u_r \Delta p_r)(x, t_{n+1})$ and barotropic momentum $(p_b \bar{u})(x, t_{n+1})$ in cell D_j by

$$(u_r \Delta p_r)^{n+1}(x) \;=\; \sum_{m=0}^{M} \left(U_{r,m}^{(j)} \right)^{n+1} \psi_m^{(j)}(x)$$

$$(p_b \bar{u})^{n+1}(x) \;=\; \sum_{m=0}^{M} \left(\overline{U_m^{(j)}} \right)^{n+1} \psi_m^{(j)}(x).$$

In analogy to (42), the consistency of these quantities is equivalent to

$$\sum_{r=1}^{L} \left(U_{r,m}^{(j)} \right)^{n+1} = \left(\overline{U_m^{(j)}} \right)^{n+1} \tag{53}$$

18

for $0 \leq m \leq M$.

Assume that equation (35) for mode m of the u-component of layer momentum is discretized with a time-stepping method of the form

$$\left(U_{r,m}^{(j)}\right)^* = \left(U_{r,m}^{(j)}\right)^n + \Delta t \left(G_{r,m}^{(j)}\right)^{n+1} \tag{54}$$

for $0 \leq m \leq M$ and $1 \leq r \leq L$, where $\left(G_{r,m}^{(j)}\right)^{n+1}$ is an approximation to the right side of (35). The quantity $\left(U_{r,m}^{(j)}\right)^*$ on the left side of (54) would be the numerical solution at time t_{n+1}, except for the need to enforce the consistency condition (53). That condition will be enforced with the modified method

$$
\begin{aligned}
\left(U_{r,m}^{(j)}\right)^{n+1} &= \left(U_{r,m}^{(j)}\right)^n + \Delta t \left(G_{r,m}^{(j)}\right)^{n+1} + (\Delta t)w_r^{(j)} \left(E_m^{(j)}\right)^{n+1} \\
&= \left(U_{r,m}^{(j)}\right)^* + (\Delta t)w_r^{(j)} \left(E_m^{(j)}\right)^{n+1},
\end{aligned}
\tag{55}
$$

where $w_1^{(j)}, \ldots, w_L^{(j)}$ are nonnegative weight coefficients with sum 1, and $\left(E_m^{(j)}\right)^{n+1}$ is a depth-independent correction term that is derived below. In the code that was used to perform the computations described in Section 6, the weights are

$$w_r^{(j)} = \left(\delta_{r,0}^{(j)}\right)^{n+1} / \left(\overline{\delta_0^{(j)}}\right)^{n+1};$$

this formulation assumes that the mass variables have already been made consistent (compare to (52)), so that the weights have sum equal to 1.

Now assume that equation (39) for mode m of the u-component of barotropic momentum is discretized by an equation of the form

$$\left(\overline{U_m^{(j)}}\right)^{n,i+1} = \left(\overline{U_m^{(j)}}\right)^{n,i} + \frac{\Delta t}{N} \left(\overline{G_m^{(j)}}\right)^{n,i+1} \tag{56}$$

for $0 \leq i \leq N-1$. Sum equation (56) for $0 \leq i \leq N-1$ and cancel some terms to obtain

$$\left(\overline{U_m^{(j)}}\right)^{n+1} = \left(\overline{U_m^{(j)}}\right)^n + \Delta t \left[\frac{1}{N} \sum_{i=0}^{N-1} \left(\overline{G_m^{(j)}}\right)^{n,i+1}\right]. \tag{57}$$

On the other hand, the vertical sum (for $1 \leq r \leq L$) of the layer method (55) is

$$\sum_{r=1}^{L} \left(U_{r,m}^{(j)}\right)^{n+1} = \sum_{r=1}^{L} \left(U_{r,m}^{(j)}\right)^n + \Delta t \sum_{r=1}^{L} \left(G_{r,m}^{(j)}\right)^{n+1} + (\Delta t) \left(E_m^{(j)}\right)^{n+1}. \tag{58}$$

A comparison of (57) and (58) shows that the consistency condition (53) for mode m is satisfied at t_{n+1}, assuming that it is already satisfied at time t_n, if and only if

$$\left(E_m^{(j)}\right)^{n+1} = -\sum_{r=1}^{L} \left(G_{r,m}^{(j)}\right)^{n+1} + \left[\frac{1}{N} \sum_{i=0}^{N-1} \left(\overline{G_m^{(j)}}\right)^{n,i+1}\right]. \tag{59}$$

19

Substitution of this result into (55) then yields a method for layer momentum that is consistent with the algorithm for the barotropic momentum.

The correction term $\left(E_m^{(j)}\right)^{n+1}$ in (59) has some properties analogous to those of the term $C^{(j)}$ in (51). In particular, the quantity (59) is due entirely to truncation error, and its usage amounts to subtracting layer r's share of the unresolved fast forcing from the layer equation and replacing it with the time average of well-resolved forcing from the barotropic equation, thus introducing a kind of time filtering into the forcing for the method (55).

In practice, the correction $\left(E_m^{(j)}\right)^{n+1}$ can be computed in a manner that is simpler than what is suggested by equation (59). Vertical summation of the layer method (55) yields

$$\sum_{r=1}^{L} \left(U_{r,m}^{(j)}\right)^{n+1} = \sum_{r=1}^{L} \left(U_{r,m}^{(j)}\right)^{*} + (\Delta t)\left(E_m^{(j)}\right)^{n+1}.$$

The consistency condition (53) is then satisfied if and only if

$$(\Delta t)\left(E_m^{(j)}\right)^{n+1} = \left(\overline{U_m^{(j)}}\right)^{n+1} - \sum_{r=1}^{L}\left(U_{r,m}^{(j)}\right)^{*}. \tag{60}$$

This result can be substituted into (55) in order to obtain the necessary adjustment to $\left(U_{r,m}^{(j)}\right)^{*}$ for $1 \le r \le L$.

A verbal description of the algorithm is the following. Use equation (54) to compute the tentative momentum variables, subtract their vertical sum from the barotropic momentum variable, and then distribute this difference over the various layers. This description may cause the method to seem like an improvisation, but the preceding analysis gives the method a systematic derivation.

4.3. A time-stepping method

This subsection outlines a time-stepping method for barotropic-baroclinic splitting of the system of governing equations considered here. This method is similar to a two-level time-stepping method developed by Higdon [10] for barotropic-baroclinic splitting in the case of finite difference and finite volume methods, but it is modified here for the present case of DG spatial discretizations.

A great deal of recent research has been devoted to developing and analyzing higher-order Runge-Kutta time-stepping methods that can be used with DG spatial discretizations. (See, e.g., Dawson et al. [4], Gottlieb et al. [8], Kubatko, et al. [18] and Seny et al [23].) However, the time-stepping method discussed here is already configured for usage with a barotropic-baroclinic time splitting, and it gives very good results in the numerical computations described in Section 6 and in the analysis and computations described in [14].

In the present discussion of time-stepping, the "barotropic" equations consist of the system (39)–(41) of ordinary differential equations that are obtained

from DG spatial discretization; the unknown quantities in this system are the time-dependent degrees of freedom in the representation (38) of the barotropic momentum and mass variables. The "baroclinic" equations consist of the equations (35)–(37) for the degrees of freedom for momentum and mass in the layers, but with the modifications described in Section 4.2 to obtain consistency with the barotropic variables. These modifications consist of equations (44)–(45) for mass, equation (55) for the u-component of momentum, and an analogous equation for the v-component of momentum.

For the sake of computing certain forcing terms, it is assumed here that the velocity components $u_r(x, t)$ and $v_r(x, t)$ and layer thickness $\Delta p_r(x, t)$ are split into barotropic and baroclinic components. (This comment applies to the pointwise functions, not to degrees of freedom.) The splitting of u is given in (18), and the splitting of v is analogous. A splitting of $\Delta p_r(x, t)$ for the case of isopycnic coordinates is described in Section 5.1.

The following algorithm describes the evolution of the system from time t_n to time $t_{n+1} = t_n + \Delta t$, where Δt is appropriate for modeling the slow motions in the system. The time interval $[t_n, t_{n+1}]$ will be regarded as a "baroclinic" time interval, and the baroclinic equations are solved explicitly with time step Δt. The fast barotropic equations are solved explicitly with time step $\Delta t/N$, where N is the number of barotropic subintervals of the baroclinic time interval. The computation of the pressure terms for the barotropic and baroclinic equations is discussed in Section 5.

The algorithm includes prediction and correction of the dependent variables.

4.3.1. Prediction steps

(1) Predict the barotropic degrees of freedom, using an algorithm that is described below. During the computation of forcing terms (i.e., mass advection, momentum advection, pressure) use baroclinic quantities from time t_n and barotropic quantities obtained during the course of the time-stepping.

(2) Predict the degrees of freedom for the masses in the layers, i.e., degrees of freedom for layer thicknesses. In the computation of the mass flux term, all time-dependent quantities are taken from time t_n. For an advective velocity at cell edges in layer r, use an unweighted average of the one-sided limits of u_r. For a mass flux at cell edges, the computations described in Section 6 use the upwind flux. At the end of this step, enforce consistency with the predicted degrees of freedom for barotropic mass at time t_{n+1}.

(3) Predict the degrees of freedom for the momentum densities in the layers. In the Coriolis and momentum advection terms, use data from time t_n. For the momentum flux at cell edges, use the upwind flux and the same advective velocity at cell edges as for the mass in step (2). For the quantities used to compute the pressure term, use baroclinic data from time t_n and time averages of predicted barotropic data over all of the barotropic substeps of the baroclinic interval $[t_n, t_{n+1}]$. Enforce consistency with the predicted barotropic momentum.

4.3.2. Correction steps

(4) Correct the barotropic degrees of freedom. When baroclinic quantities are needed during the computation of forcing terms, use unweighted time averages from times t_n and t_{n+1}.

(5) Correct the degrees of freedom for the masses in the layers. During the computation of the advective velocity at cell edges and mass fluxes at interior quadrature points, use unweighted averages of baroclinic quantities at times t_n and t_{n+1} and time averages of corrected barotropic quantities over all substeps of $[t_n, t_{n+1}]$. Enforce consistency with the corrected degrees of freedom for barotropic mass at time t_{n+1}.

(6) Correct the degrees of freedom for the momentum densities in the layers. During the computation of forcing terms (except the Coriolis terms), use time averages of baroclinic and barotropic quantities. Represent the Coriolis terms with unweighted averages of degrees of freedom from times t_n and t_{n+1}, so that the Coriolis terms are implemented implicitly; for each mode and each grid cell, this requires the solution of a 2×2 linear system. Enforce consistency with the corrected barotropic momentum.

4.3.3. Time-stepping for the barotropic equations

The barotropic equations can be solved with a method that follows the same general outline as the method described above for the overall barotropic-baroclinic splitting, but simplified to fit the barotropic system. That is, at each barotropic substep, predict the degrees of freedom for barotropic mass and momentum with forward steps, and then correct with steps that employ unweighted time averages in the forcing terms. All parts of the algorithm are explicit, except for an implicit representation of the Coriolis terms.

In equation (39) for the degrees of freedom in the u-component of barotropic momentum, the advection term (21) includes the vertically-integrated momentum flux

$$Q_u(x, t) = \bar{u}(p_b \bar{u}) + p_b \left(\sum_{r=1}^{L} u_r' u_r' \frac{\Delta p_r}{p_b} \right) \tag{61}$$

stated in (22). In the case of isopycnic coordinates, which are used in Sections 5 and 6, the ratio $\Delta p_r / p_b$ is purely baroclinic, and in that case the quantity in parentheses in (61) varies essentially on the slow time scale. Denote that quantity by Q_u^{bcl}. Due to its slow variation, the quantity Q_u^{bcl} can be held constant in time during the barotropic time integration. When the barotropic equations are solved during the prediction step of the overall barotropic-baroclinic algorithm, evaluate Q_u^{bcl} at time t_n; during the correction step for the overall algorithm, use an average of values from times t_n and t_{n+1}.

At cell edges, the term $\bar{u}(p_b \bar{u})$ can be discretized with an upwind flux, where $\bar{u}$ serves as an advective velocity and $p_b \bar{u}$ serves as a momentum density. At such edges, use an average of one-sided limits of Q_u^{bcl} and a Lax-Friedrichs interpolation of the coefficient p_b; the latter process is discussed in Section 5.2.

5. Computation of pressure at cell edges

The integral weak form (9) of the pressure forcing in the u-momentum equation includes a vertical integral $H_r(x,t)$ (in (10)–(11)) of the pressure. If x is in the interior of a grid cell, then this integral is well-defined. However, at a cell edge the pressure may be discontinuous, in a DG discretization, so in that case there is ambiguity about the value of pressure and thus ambiguity about the value of H_r. If this ambiguity is not resolved then the numerical method could, in effect, violate Newton's third law of motion.

A standard approach to determining solution values at a cell edge is to solve a Riemann problem (e.g., LeVeque [19]), in which one-sided limits of the solution are used to define a piecewise constant initial state; the dynamics of the system of partial differential equations then gives values of the dependent variables at the cell edge. However, an ocean circulation model could have many layers (e.g., dozens), and if the hydrostatic condition is assumed then those layers are strongly coupled in the vertical direction. In this case, a Riemann problem could be highly complicated. The present section describes how some ideas related to barotropic-baroclinic splitting can be used to confine the Riemann problem to a simpler system of lower spatial dimension and thus facilitate the process of computing the pressure at cell edges.

In the present discussion, it is assumed that the vertical coordinate is an isopycnic coordinate and that a vertical discretization divides the fluid into layers of constant density. Let α_r denote the specific volume (reciprocal of density) in layer r, for $1 \le r \le L$, where r increases downward. Thus $\alpha_1 > \alpha_2 > \ldots > \alpha_L$.

5.1. Pressure splitting

It is first necessary to develop a splitting of the pressure field into barotropic and baroclinic components. (A splitting of velocity is given in (18).) The quantity $p_b(x,t)$ defined in (15) is equal to g times the mass per unit horizontal area in the water column; the pressure at the bottom of the fluid is then $p_b(x,t)$ plus the atmospheric pressure at the top of the fluid. Now let $p_b'(x)$ be the value of $p_b(x,t)$ when the fluid is at the global rest state consisting of zero velocity and a level free surface and level interfaces between layers. (Here, a prime (') does not denote differentiation.) Define $\eta(x,t)$ to be the relative perturbation of $p_b(x,t)$ from its rest value; i.e.,

$$\eta(x,t) = \frac{p_b(x,t) - p_b'(x)}{p_b'(x)}. \tag{62}$$

Then

$$p_b(x,t) = \Big(1 + \eta(x,t)\Big)p_b'(x), \tag{63}$$

and $p_b'\eta$ is the perturbation in water column mass (times g) from its rest value. The quantity $p_b'\eta$ is also the perturbation in bottom pressure. Given the definition (62) of η, and given the vertical pressure increment $\Delta p_r(x,t)$ across layer

r (from (4)), define $\Delta p'_r(x, t)$ so that

$$\Delta p_r(x, t) = \Big(1 + \eta(x, t)\Big)\Delta p'_r(x, t). \tag{64}$$

It follows from (15), (63), and (64) that

$$\sum_{r=1}^{L} \Delta p'_r(x, t) = p'_b(x). \tag{65}$$

The splitting in (64) is due to Bleck and Smith [3], and it is based on the idea that an external signal causes all fluid layers to thicken or thin by approximately the same proportion. The factor $1 + \eta$ represents this thickening or thinning, and the remaining factor $\Delta p'_r$ (approximately) represents the internal motions. The quantity $\Delta p'_r$ thus varies (approximately) on the slow time scale, and it can be regarded as the baroclinic component of the layer thickness. The quantities p_b and η can vary on the fast time scale and can be regarded as barotropic variables.

Now define $p'_0 = 0$, and let p_0 be the atmospheric pressure. Summation of (64) over layers 1 through r yields

$$p_r(x, t) = p_0 + \Big(1 + \eta(x, t)\Big)p'_r(x, t) \tag{66}$$

for $0 \leq r \leq L$. Here, p_r and p'_r denote the total and baroclinic pressures, respectively, at the bottom of layer r for $1 \leq r \leq L$. If p_0 is constant, then according to some remarks in Section 5.1 of [14], p_0 can be subtracted from the fluid pressure during the derivation of the pressure forcing term (9). After a substitution of notation, one can then use $p_0 = 0$ in the resulting formulas. In those formulas, one can also use the splitting

$$p_r(x, t) = \Big(1 + \eta(x, t)\Big)p'_r(x, t) \tag{67}$$

in place of (66).

The definition of $\Delta p'$ in (64) is stated in terms of vertical pressure increments between layer interfaces, but the same relation can be used for any two points in the fluid that have the same horizontal position. The relations (66) and (67) can be extended similarly. The notation in (64), (66), and (67) is used here because the primary usage of these formulas will be in relation to layer interfaces.

5.2. Riemann problem and Lax-Friedrichs interpolation

The analysis given below requires values of η at cell edges, and this suggests the usage of a Riemann problem. (The method stated here actually computes $p'_b\eta$, as this can be expressed in terms of conserved quantities that are dependent variables in the system, and a division then yields η.) For purposes of determining quantities at a cell edge, the Riemann solution is used only in a neighborhood of the cell edge and for values of t that are arbitrarily close to,

but later than, the time when the piecewise constant initial state is imposed. The following discussion is thus local in both space and time.

As noted in Section 3.3, the barotropic equations are similar to the shallow water equations, and their dynamics are nearly linear in the sense described in that section. For the short-time behavior that is necessary to obtain a suitable value of $p_b'\eta$ at a cell edge, we will employ the linearized shallow water equations with the Coriolis term f set to zero. The solution of this system is derived via the method of characteristics in Section 5.6 of [14], and in that section it is pointed out that if this solution is used to obtain a mass flux for the linearized system, the resulting flux is the Lax-Friedrichs flux. For the present case of $p_b'\eta$, the calculations in [14] suggest

$$(p_b'\eta)_{j-1/2}^{LF} = \frac{1}{2}\Big[(p_b'\eta)_- + (p_b'\eta)_+\Big] + \frac{1}{2c}\Big[(p_b\bar{u})_- - (p_b\bar{u})_+\Big] \qquad (68)$$

for a value of $p_b'\eta$ at the cell edge $x_{j-1/2}$ between cells D_{j-1} and D_j. Here, the subscripts $-$ and $+$ refer to left and right limits from within cells D_{j-1} and D_j, respectively, and dependences on t are not included in the notation. The quantity c is the local gravity wave speed, i.e., $c = \sqrt{gh}$, where h is the mean depth of the fluid at the cell edge. The result (68) will be regarded as a "Lax-Friedrichs interpolation" of the quantity $p_b'\eta$ at cell edge $x_{j-1/2}$.

In the case where the elevation of the bottom topography is not constant, the elevation (and thus p_b') could be discontinuous at cell edges. In that event, define an edge value $(p_b')_{j-1/2}$ to be the minimum of the left and right limits of p_b' at the cell edge; equivalently, let the elevation at the edge be the maximum of the left and right limits of the elevations within cells D_{j-1} and D_j. Use $(p_b')_{j-1/2}$ in the definition (62) of η at the cell edge; and for the quantities $(p_b\bar{u})_-$ and $(p_b\bar{u})_+$ in (68), use the ratios $(p_b')_{j-1/2}/(p_b')_-$ and $(p_b')_{j-1/2}/(p_b')_+$ to determine the momentum in the portion of the fluid that lies above the elevation of the edge. The preceding ideas are analogous to some ideas discussed in Section 5.3 of [14] for the case of the shallow water equations.

For the Riemann solution considered here, the method of characteristics shows that discontinuities propagate with velocities c and $-c$ from the location of the initial discontinuity. This pattern is then found in the quantity $1 + \eta$, which represents the thickening or thinning of the layers in a multi-layer model. Figure 2 shows an example of such a pattern, for a purely external mode.

Next consider the effect of a Riemann solution for $1 + \eta$ on a general fluid state. An example is illustrated in Figure 3. In a DG representation, the baroclinic layer thicknesses $\Delta p_r'$ can be discontinuous across the cell edge $x_{j-1/2}$, and consequently the interior layer interfaces in a baroclinic state can also be discontinuous across that edge. The total layer thicknesses Δp_r are obtained by multiplying $\Delta p_r'$ by $1 + \eta$, as in (64). In the resulting state, the discontinuities of the interior interfaces across the cell edge are maintained. In addition, the moving discontinuities in $1 + \eta$ introduce discontinuities in layer thicknesses, interface elevations, and free-surface elevation that propagate across the adjacent cells.
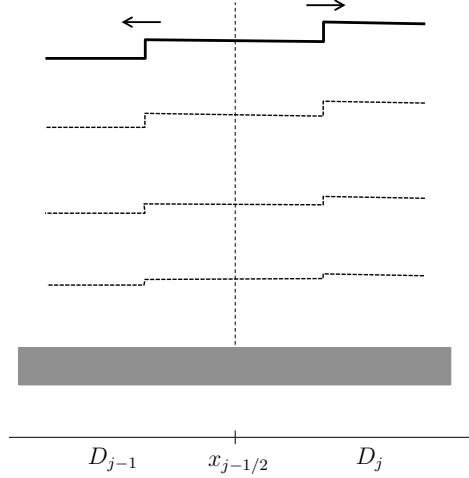
Figure 2: Riemann solution for the barotropic quantity $1 + \eta$. In a multi-layer model this quantity represents the proportional thickening or thinning of layers, and it closely approximates the behavior of the mass field in the external mode. The present figure illustrates an example of $1 + \eta$ in terms of perturbations of a multi-layer fluid from its rest state. The horizontal lines show the free surface and the interfaces between the layers, and the shaded region indicates the bottom of the fluid region. The vertical line shows the location $x_{j-1/2}$ of the initial discontinuity. The discontinuities in $1 + \eta$ propagate with velocities c and $-c$ from that location.

However, at the cell edge $x_{j-1/2}$ the elevation of the free surface is (nearly) continuous, as illustrated in the configuration shown in Figure 3. To be more precise, the change in elevation from the bottom to the top of the fluid is

$$\sum_{r=1}^{L} \Delta z_r \;=\; \sum_{r=1}^{L} (\alpha_r/g)\Delta p_r \;=\; (1+\eta)\sum_{r=1}^{L} (\alpha_r/g)\Delta p_r'. \tag{69}$$

(The first equality follows from the hydrostatic condition.) For the moment, assume that the elevation of the bottom topography is continuous across a cell edge. The quantity $1 + \eta$ is continuous across the edge, due to the nature of the Riemann solution. The quantity $\sum_{r=1}^{L} \Delta p_r'(x,t)$ is simply $p_b'(x)$ (see (65)); this is the value of p_b at the global rest state, and it is continuous if the bottom topography is continuous. Any discontinuity in the quantity $\sum_{r=1}^{L} (\alpha_r/g)\Delta p_r'$ is therefore due to jumps in the elevations of interfaces, combined with density contrasts across layers. However, at any horizontal location the variation in density over the entire depth of the fluid is on the order of one percent, so any discontinuities in (69) are likely to be very small. In the case where the bottom topography is discontinuous at a cell edge, the preceding argument can be extended by using ideas analogous to those used in the paragraph after equation (68).
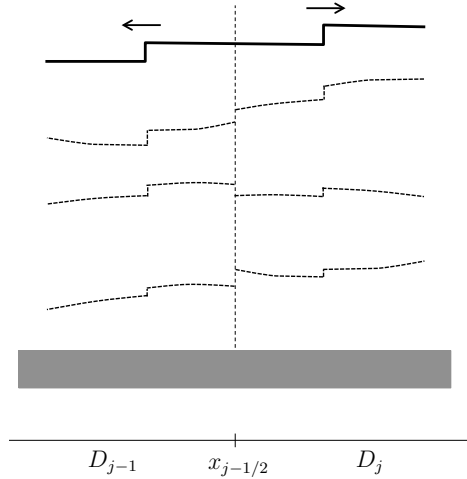
Figure 3: Layer structure when a purely baroclinic state is combined with a Riemann solution for the barotropic quantity $1 + \eta$. The baroclinic layer thicknesses and interior interface elevations can be discontinuous across the cell edge $x_{j-1/2}$. The total layer thicknesses are obtained by multiplying the baroclinic layer thicknesses by $1 + \eta$. For a baroclinic state, the free surface is (essentially) continuous everywhere. Since the Riemann solution for $1 + \eta$ is continuous at the cell edge, the free surface in the state illustrated here is also (essentially) continuous at the cell edge. For purposes of determining quantities at a cell edge, the Riemann solution is used only in a neighborhood of that edge.

The algorithm described in the next subsection employs the conjecture that any discontinuities in the free surface are so small that they may be neglected during the development of that algorithm.

5.3. Computation of vertically-integrated pressure

We now address the computation of the quantity $H_r(x, t)$ in (10)–(11), which is repeated here as

$$H_r(x, t) \;\; = \;\; g \int_{z_r(x,t)}^{z_{r-1}(x,t)} P(x, z, t) \; dz \tag{70}$$

$$= \;\; \int_{p_{r-1}(x,t)}^{p_r(x,t)} \alpha \, p \; dp. \tag{71}$$

The present discussion is concerned mainly with the computation of $H_r(x, t)$ in the context of solving the baroclinic equations with long time steps. At the end of this subsection are some remarks on computing the vertical sum of $H_r(x, t)$ when the vertically-integrated barotropic equations are solved with short time steps.

At quadrature points in the interiors of grid cells, the quantity $H_r(x, t)$ is well-defined and can be computed with the form (71). However, in the case

where H_r is used to solve the baroclinic equations on a baroclinic time interval $[t_n, t_{n+1}]$, it is advisable to split the pressure field into barotropic and baroclinic components. For convenience, assume that the atmospheric pressure is constant, so that one can set $p_0 = 0$ and use the splitting (67) of the pressure. In the case of constant α the representation (71) becomes

$$\frac{1}{2}\alpha(1 + \eta)^2 \left[(p'_r)^2 - (p'_{r-1})^2\right].\tag{72}$$

When this expression is implemented, use time averages of $(1 + \eta)^2$ over all barotropic substeps in order to avoid the aliasing of fast motions onto the coarse baroclinic time grid. On the other hand, the baroclinic state varies slowly in time, and the values of p' can be values from time t_n during a prediction step and an average of values from times t_n and t_{n+1} during a correction step.

Next consider the computation of pressure, and then H_r, at cell edges. For definiteness, consider the pressure at the edge $x_{j-1/2}$ between cells D_{j-1} and D_j. To determine the pressure at that edge, consider the mass field obtained by combining a baroclinic state with a Riemann solution for the barotropic quantity $1 + \eta$. The combination of $1 + \eta$ with a baroclinic state yields a mass field of the kind illustrated in Figure 3.

In such a configuration, the free surface is (essentially) continuous across the cell edge $x_{j-1/2}$, but the layer interfaces need not be continuous across that edge. Because of the density contrasts between layers, the pressure could therefore be discontinuous in x across the edge; however, the jump in pressure across the edge for fixed z is typically small, due to the relatively small vertical variation of density that is mentioned near the end of the preceding subsection. At the edge $x_{j-1/2}$, let $p'_+(z)$ and $p'_-(z)$ denote the right and left limits of p', respectively. Also let η_{LF} denote the Lax-Friedrichs interpolation of η at that edge; this interpolation is obtained by evaluating the Riemann solution at $x_{j-1/2}$, as described in Section 5.2. (For the sake of simplicity, dependences on j and t are not included in this notation.) The right and left limits of total pressure at this edge are then

$$P_+(z) = p'_+(z)\left(1 + \eta_{LF}\right)\tag{73}$$

$$P_-(z) = p'_-(z)\left(1 + \eta_{LF}\right),\tag{74}$$

respectively. For an approximation to the total pressure at the edge, let

$$P(z) = \frac{1}{2}\left(P_+(z) + P_-(z)\right)$$
$$= \frac{1}{2}\left(p'_+(z) + p'_-(z)\right)\left(1 + \eta_{LF}\right).\tag{75}$$

Any differences between $P_+(z)$ and $P_-(z)$ are typically small, and the following derivation relies on the assumption that the simple average in (75) is adequate for determining a pressure that can be used to compute H_r at a cell edge.

28

The pressures (73) and (74) yield vertical pressure increments between layer interfaces on either side of the edge $x_{j-1/2}$. Since each layer has constant density, the hydrostatic relation $\Delta p = \rho g \Delta z$ yields differences in elevation between interfaces, which in turn yield the elevations of interfaces on each side of the cell edge. Here, "elevation" refers to elevations of interfaces in a fluid state that combines a baroclinic solution with a Riemann solution for $1 + \eta$, such as the state illustrated in Figure 3.

In a numerical implementation of the weak form (9) of the pressure forcing in cell $D_j = [x_{j-1/2}, x_{j+1/2}]$, the contribution from the pressure along the edge $x_{j-1/2}$ can be represented by

$$(H_r)_{j-1/2} \;=\; g \int_{z_r^+}^{z_{r-1}^+} P(z) \; dz. \tag{76}$$

Here, $P(z)$ is given in (75); and z_r^+ and z_{r-1}^+ are the elevations of the bottom and top of layer r in cell D_j, in the limit $x \to x_{j-1/2}^+$, as determined with the procedure that is outlined above. For later reference, also let p_1^+, ..., p_L^+ denote the corresponding total pressures at each interface, in the limit $x \to x_{j-1/2}^+$. Thus $p_r^+ = (1 + \eta_{LF}){p_r'}^+$, where ${p_r'}^+$ is the right limit of p' along interface r. Now insert (75) into (76) to obtain

$$(H_r)_{j-1/2} \;=\; \frac{1}{2} g \int_{z_r^+}^{z_{r-1}^+} P_+(z) \; dz \;+\; \frac{1}{2} g \int_{z_r^+}^{z_{r-1}^+} P_-(z) \; dz. \tag{77}$$

For the first integral on the right side of (77), the interval of integration is the entire vertical extent of layer r in cell D_j, in the limit $x \to x_{j-1/2}^+$. This integral can be converted into an integral with respect to p, in the manner of (71), so that the first term on the right side of (77) is

$$
\begin{aligned}
\frac{1}{2} g \int_{z_r^+}^{z_{r-1}^+} P_+(z) \; dz \;&=\; \frac{1}{2} \int_{p_{r-1}^+}^{p_r^+} \alpha p \; dp \\
&=\; \frac{1}{2} \alpha_r \left((p_r^+)^2 - (p_{r-1}^+)^2 \right) \\
&=\; \frac{1}{2} \alpha_r \left(1 + \eta_{LF} \right)^2 \left(({p_r'}^+)^2 - ({p_{r-1}'}^+)^2 \right). \tag{78}
\end{aligned}
$$

The second equality uses the assumption that layer r has a constant specific volume α_r. In the last expression, use time averages of $(1 + \eta_{LF})^2$ over all barotropic substeps.

In general, the evaluation of the second integral on the right side of (77) can be more complicated the evaluation of the first integral. The values of the integrand $P_-(z)$ are defined in (74) and involve the left-hand limits of p', which depend on values of p' from within the neighboring cell D_{j-1}. In analogy to the elevations z_0^+, ..., z_L^+ of interfaces in the limit $x \to x_{j-1/2}^+$ from within cell D_j, define elevations z_0^-, ..., z_L^- of interfaces in the limit $x \to x_{j-1/2}^-$ from within

29

cell D_{j-1}. The elevations z_0^-, ..., z_L^- need not coincide with the elevations z_0^+, ..., z_L^+, due to possible discontinuities in p' across the cell edge. Accordingly, the evaluation of the second integral on the right side of (77) requires that the interval of integration $[z_r^+, z_{r-1}^+]$ be divided into subintervals, each of which is an intersection of $[z_r^+, z_{r-1}^+]$ with an interval of the form $[z_q^-, z_{q-1}^-]$ for $1 \leq q \leq L$. The integral on each such subinterval is evaluated in a manner that is an analogue of (78).

In a fluid state that combines a baroclinic state with a Riemann solution for $1 + \eta$, as illustrated in Figure 3, the top and bottom of layer r can contain short vertical segments within the interiors of grid cells D_{j-1} and D_j. Integrals of pressure over those segments should therefore be included in the representation of the pressure term (9). In the limit $t \to \bar{t}^+$, where $\bar{t}$ is the time where the Riemann problem is posed, the discontinuities migrate to the cell edge $x_{j-1/2}$. The integrals over the short vertical segments can therefore be expressed in terms of one-sided limits of pressures and elevations from within the cells D_{j-1} and D_j. The formulas are analogues of those given above, so the details are omitted here.

In the representation (77), the two integrals have the same limits of integration. This representation thus assumes that the fluid regions on each side of the cell edge are in contact over the entire extent of the vertical interval $z_r^+ \leq z \leq z_{r-1}^+$. This assumption is enabled by the fact that the free surface is (essentially) continuous when the Riemann solution for $1 + \eta$ is combined with the baroclinic state, as illustrated in Figure 3, and this circumstance relies on the usage of the barotropic-baroclinic splitting. In contrast, without such a splitting one encounters a discontinuous configuration like that shown in Figure 1, and it is necessary to deal with the possibility that the fluid in one cell may extend above the fluid in the neighboring cell. Aizinger and Dawson [1] treat this problem by smoothing the free surface, but such a procedure is not needed when a barotropic-baroclinic splitting is used.

Next consider the computation of the pressure term for the vertically-integrated barotropic equations. In this case one uses the quantity $H(x,t) = \sum_{r=1}^{L} H_r(x,t)$ given in equation (25). At quadrature points in the interiors of grid cells, use the vertical sum of the quantity (72). That sum involves a vertical sum of terms involving p'; this baroclinic sum is held constant during a barotropic integration, while the factor $(1 + \eta)^2$ is updated at each barotropic time step. On the other hand, at a cell edge use a vertical sum of the quantity $(H_r)_{j-1/2}$ in (77); this includes a vertical sum of (78) and its analogue for left-hand limits. One then obtains a baroclinic quantity times the factor $(1 + \eta_{LF})^2$, which is updated at each barotropic time step.

6. Numerical computations

The present section describes some numerical computations that test the ideas developed in the preceding sections.

The test problems used here involve the process of geostrophic adjustment. Oceanic flows are typically close to a state of geostrophic balance, i.e., the

Coriolis terms and pressure forcing terms in the momentum equations are nearly equal; when viewed from above, the fluid at each elevation flows along curves of constant pressure. If the fluid departs from such a state, such as when the densities of some fluid regions are altered due to temperature changes or freshwater inputs, then the system tends to adjust to a geostrophically-balanced state of some nature. During the adjustment process, the difference between the present state and the future balanced state propagates away in the form of wave motions.

In the analysis and numerical computations reported in [14], the DG algorithms developed in that paper were found to provide highly accurate simulations of inertia-gravity waves, whereas this is not always the case with finite difference methods based on the staggered B- and C-grids that have traditionally been used in ocean modeling. These results were stated in terms of the single-layer shallow water equations, but the velocity and length scales in those results make them pertinent to internal motions in a multi-layer fluid. These results suggest that DG methods might be effective in simulating geostrophic adjustment, and the purpose of the present computations is to test this idea for a multi-layer fluid.

6.1. Problem configuration

For each of the computations described here, the initial state consists of zero velocity and piecewise constant layer thicknesses, and the final steady state is a geostrophically-balanced solution having a form derived in the Appendix. In each case, the initial layer thicknesses are determined by an eigenvector of the eigenvalue problem (A.17) associated with modal solutions (A.11) of the linearized equations for a multi-layer fluid. One such mode is the external mode, and the others are internal modes. Different modes are thus tested individually in these computations.

In the configuration used here, the fluid consists of 10 layers having specific volumes ranging downward from 0.975×10^{-3} m^3/kg to 0.972×10^{-3} m^3/kg in equally-spaced increments. When the system is at the rest state consisting of zero velocity and level interfaces and a level free surface, the layer thicknesses (in meters) are 20, 30, 45, 60, 80, 100, 125, 150, 180, 210, ordered from top to bottom, for a total depth of 1000 meters.

As assumed in earlier sections of this paper, all flow variables are independent of y, and the Coriolis parameter is nonzero and constant. Solutions are computed on spatial intervals of the form $-x_{max} \leq x \leq x_{max}$, with solid-wall boundary conditions at the ends. Solutions are plotted on smaller subintervals. In each computation, x_{max} is chosen large enough so that any reflections from the solid walls are not visible in the display intervals during the time interval of integration. This problem configuration can be regarded as modeling a fluid flow in an infinite straight channel in a rotating reference frame.

For the modal solutions derived in the Appendix, the speed of inertia-gravity waves in mode j in the nondispersive limit is

$$c^{(j)} = \frac{c}{\sqrt{\lambda^{(j)}}}, \tag{79}$$

where $c = \sqrt{\alpha_L \tilde{p}_L}$ (see (A.16)); $\lambda^{(0)}$, $\lambda^{(1)}$, ..., $\lambda^{(L-1)}$ are the (dimensionless) eigenvalues of (A.17); $j = 0$ refers to the external mode; and $1 \leq j \leq L-1$ refers to the internal modes. (Here, $L = 10$.) For the example considered here, $c \approx 99.00$ m/sec, $\lambda^{(0)} \approx 0.9995$, and $\lambda^{(1)}$, ..., $\lambda^{(9)}$ range from approximately 3.64×10^3 to approximately 3.16×10^5. Thus $c^{(0)} \approx 99.02$ m/sec, and $c^{(1)}$, ..., $c^{(9)}$ range from 1.64 m/sec down to 0.18 m/sec.

The exact solutions derived in the Appendix involve the Rossby radius of deformation (A.27), a length scale associated with the deformation of the layer interfaces in the geostrophically-balanced state. For mode j, this quantity is

$$R^{(j)} = \frac{c^{(j)}}{f}, \tag{80}$$

where f is the Coriolis parameter. In these computations $f = 10^{-4}$ sec^{-1}, so $R^{(0)} \approx 990$ km, and $R^{(1)}$, ..., $R^{(9)}$ range from 16.4 km to 1.8 km. A plot of the internal Rossby radii is given in Figure 4.
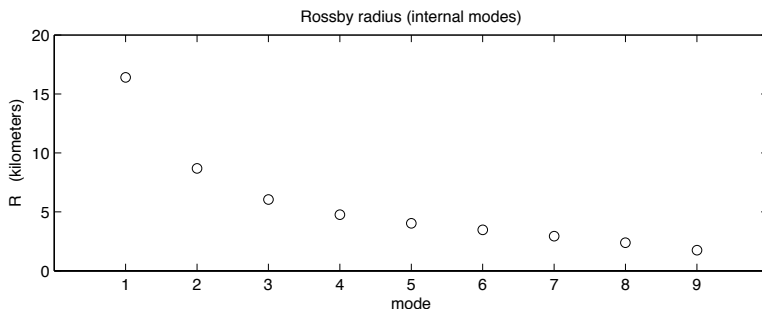

Figure 4: Rossby radius of deformation, in kilometers, for the internal modes ($1 \leq j \leq 9$) in the example considered here. For the external mode ($j = 0$), the Rossby radius is approximately 990 km.

For modal solutions, the vertical dependences of the horizontal velocity components and of the relative perturbations in layer thickness are determined by the eigenvectors of (A.17). In the case of the external mode ($j = 0$), the vertical dependence is very close to uniform; for the example considered here, the relative variation in the components is approximately 0.1%. In the case of the internal modes, the components of the eigenvectors oscillate, with the rate of oscillation increasing as j increases. This is a discrete analogue of the behavior of eigenfunctions for the continuous case that is discussed, for example, in [11].

For the initial conditions used here, the relative perturbation in layer thickness at time $t = 0$ is given in (A.30). In that equation, ϵ is a dimensionless constant of either sign, and ϕ_r is component r of the eigenvector ϕ. In these computations, each eigenvector is normalized so that the maximum of the absolute values of the components is 1; $|\epsilon|$ is thus equal to the maximum relative perturbation in layer thickness at the initial time. For the computations involving internal modes that are described in Sections 6.2–6.4, the value $\epsilon = 0.01$

was used. Some larger values of ϵ were also tested (e.g., 0.1, 0.2, 0.3), and for these values the computed solutions seemed reasonable. However, results with the smaller value $\epsilon = 0.01$ are shown here in order to enable comparisons to exact solutions of the linearized equations.

The computations described here use a code based on the discontinuous Galerkin algorithms described in previous sections of this paper. For these computations, the grid cells have uniform width $\Delta x = 10$ km, and piecewise quadratic functions are used to approximate the spatial dependence in each of the dependent variables. For the barotropic equations the time step is $\Delta t_{btp} = 16$ sec, and for the baroclinic equations the time step is $\Delta t_{bcl} = 960$ sec. The Courant number for the barotropic equations is then $\nu^{(0)} = c^{(0)} \Delta t_{btp} / \Delta x = 0.158$, and the Courant number for the baroclinic equations is $\nu^{(1)} = c^{(1)} \Delta t_{bcl} / \Delta x = 0.157$.

The two-level time-stepping method used for the barotropic equations is described in Section 4.3 and is the same as the one described in [14] for the shallow water equations. A stability analysis in that paper showed that this method is stable for those equations if the Courant number is at most 0.16, in the case of piecewise quadratic spatial approximations. In some numerical computations described in [14], this method gave results that were highly accurate, and the net efficiency is similar to that of higher-order methods with longer time steps. The time-stepping method used here for the overall barotropic-baroclinic splitting is a direct generalization of the method used for the barotropic equations and is also described in Section 4.3.

In the following discussions, the results obtained with the DG code are compared to results obtained with a code that uses finite difference and finite volume methods on a staggered rectangular C-grid. (On a C-grid, normal components of velocity are defined at the centers of edges of mass cells.) This C-grid code was used to obtain the numerical results reported in [10], and the algorithms in the code are described in detail in that reference. In particular, the C-grid code uses a barotropic-baroclinic time splitting and a two-level time-stepping method that is similar to the one described in Section 4.3 of the present paper.

6.2. First internal mode

Computational results will be shown here for individual modal solutions. First consider the mode corresponding to $j = 1$; this is the internal mode with smallest eigenvalue and largest wave velocity. For this mode, Figure 5 shows a side view of the fluid. The horizontal dashed lines show the positions of the free surface and the layer interfaces at the initial time, and the solid curves show those positions in the corresponding geostropically-balanced steady state. For this mode, the free surface is essentially level, and the wave motion is manifested by undulations of interfaces within the fluid.

For the sake of reducing clutter in the plot, Figure 5 shows only the top 120 meters of the fluid (out of 1000 meters), so that only the top three interfaces (out of nine) are shown. Also, the perturbations of the elevations of the free surface and the interfaces from their rest positions are multiplied by 20, for the sake of visibility. For the discontinuous elevations in the initial state, the

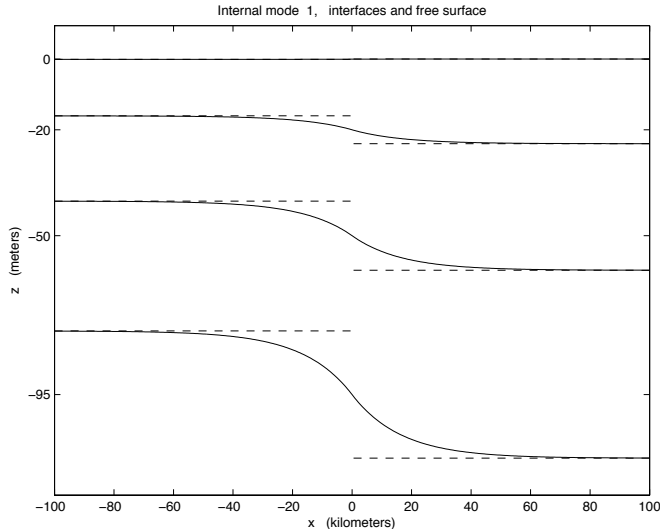Internal mode 1,   interfaces and free surface

Figure 5: Side view of the top 120 meters of the fluid, for the first internal mode ($j = 1$). The horizontal dashed lines show the positions of the free surface and the top three interfaces at the initial time, and the solid curves show those positions in the geostrophically-balanced steady state. In this plot, the perturbations from the rest states are multiplied by 20 for the sake of visibility.

maximum jump is actually approximately 4.8 meters, for the case $\epsilon = 0.01$ that is used here. (In the case $\epsilon = 0.3$ mentioned above, the jumps are so large that some of the layers are completely disconnected at the location of the jump.)

Figure 6 shows the corresponding y-component v of velocity, as a function of x, in the top layer in the geostrophically-balanced steady state. The vertical dashed lines are located at $x = \pm R^{(1)}$, where $R^{(1)}$ is the Rossby radius for mode 1. The graphs of v in the other layers have the same basic shape, so only one layer is shown. Relative to the cross-section of the fluid shown in Figure 5, v is the component of velocity into the page. In the geostrophic state, the velocity is proportional to the pressure forcing (see, e.g., the steady-state version of (A.1)), so v is maximal where the interfaces are steepest. For the small parameter value $\epsilon = 0.01$ used here, the maximum value of v is approximately 1.6 cm/sec; larger values of ϵ would yield steeper interfaces and thus larger values of v. In the steady state, the x-component of velocity is $u = 0$.

Figure 7 shows values of v in the top layer as computed with the DG code. In the top frame of that figure, the solid curve shows the computed values of v at the end of model day 10 (i.e., after 900 baroclinic time steps and 54000 barotropic steps), and the dashed curve shows the exact geostrophically-balanced steady-state solution. The solid curve shows dispersive waves radiating away from the location $x = 0$ where the initial state is discontinuous. The middle frame in Figure 7 is the same as the top frame, except that a shorter spatial interval is
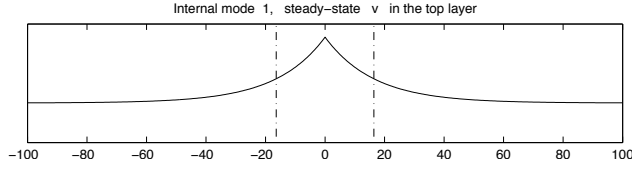
Figure 6: Velocity component v in the geostrophically-balanced steady state for the first internal mode. Relative to the cross-section shown in Figure 5, v is the component of velocity into the page. The vertical dashed lines are located at $x = \pm R^{(1)}$, where $R^{(1)}$ is the Rossby radius for this mode.

shown. In this frame the solid and dashed curves do not coincide. However, the solid curve shows a snapshot at one instant, whereas the remarks after equations (A.22)–(A.24) in the Appendix indicate that the solution oscillates in time with an angular frequency approximately equal to f. In the bottom frame in the figure, the solid curve shows a time average of v over 65 baroclinic time steps (which approximates the inertial period $2\pi/f$), beginning at the end of model day 10. This averaging removes the effect of the oscillation, and the resulting graph agrees very closely with the exact steady state. Plots of the solution at later times (not shown here) show that the magnitude of this oscillation decays as $t \to \infty$.
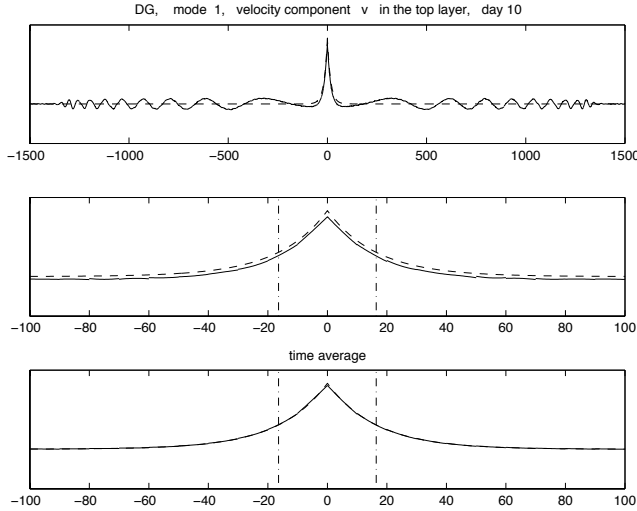

Figure 7: Values of v for the first internal mode, as computed with the DG code. In the top frame, the solid curve shows v at the end of model day 10, and the dashed curve shows the geostrophically-balanced steady state. The units on the horizontal axis are kilometers. The middle frame is the same as the top frame, except that a smaller spatial interval is used. In the bottom frame, the solid curve shows a time average of v over one inertial period beginning at the end of model day 10.

35

For a comparison, Figure 8 shows results obtained with the C-grid code that is mentioned at the end of Section 6.1. The three frames in this figure have the same format as the frames in Figure 7, except that circles are used to plot the numerical results in the lower two frames; the finite difference method produces pointwise values at grid points, and the circles illustrate what was actually computed. At the grid points, the time average shows good agreement with the exact steady state. For this computation, the grid size is $\Delta x = 10$ km, as with the computation with the DG code. However, in the present case the barotropic and baroclinic time steps are 80 sec and 4800 sec, respectively, which are much longer than those used in the DG computations. Some remarks on accuracy and efficiency are given in Section 6.4.
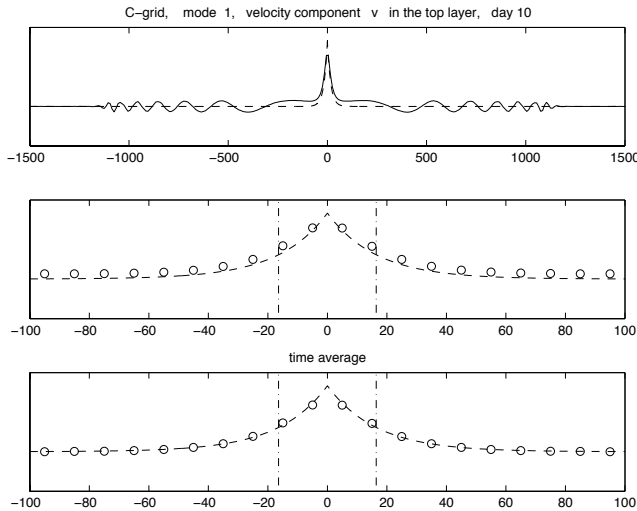

Figure 8: Values of v for the first internal mode, as computed with a C-grid code. The plotting format is the same as in Figure 7, except that circles are used in the middle and bottom frames to show the pointwise values that are computed at the grid points.

6.3. Fourth internal mode

Next consider the mode corresponding to $j = 4$; this is the internal mode with the fourth-largest wave velocity. Figure 9 shows the values of v at model day 20 as computed with the DG code, along with the exact steady-state solution. This figure has the same format as Figure 7, and the results seen in the two figures are similar. In the case of the present figure, the waves propagate away from the location $x = 0$ more slowly, as expected. Again, the DG code provides an accurate simulation of geostrophic adjustment.

In contrast, Figure 10 shows results obtained with the C-grid code that is mentioned above. The top frame in the figure shows that, by model day 20, the wave energy has propagated only a relatively short distance, and the middle
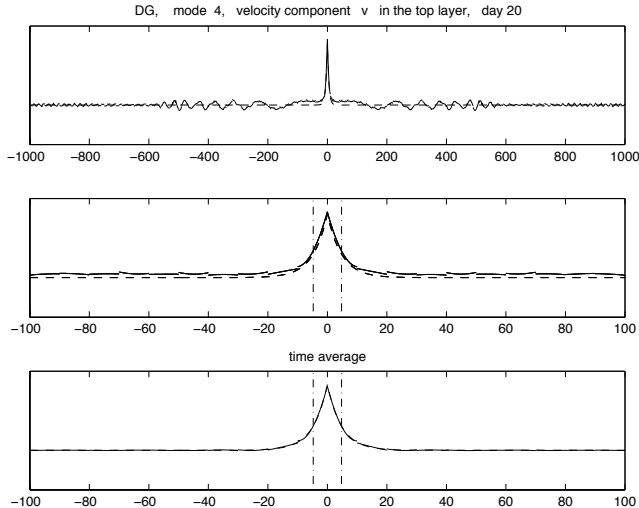
Figure 9: Values of v for the fourth internal mode ($j = 4$), as computed with the DG code. The plotting format is the same as in Figure 7, except that the solution is shown at the end of model day 20.

frame shows some pointwise values that differ greatly from the steady-state solution. The time averages shown in the bottom frame show better agreement, but a time series at a fixed location (not shown) reveals a persistent oscillation; the wave energy essentially sits there, without a proper adjustment of the kind produced by the DG code.

This behavior can be explained by considering the group velocities in numerical methods and their relation to Rossby radii and grid size. For the modal solutions considered here, the dependence with respect to (x, t) is described by the system (A.22)–(A.24), which has the structure of the linearized shallow water equations. Analyses of numerical methods for the shallow water system can therefore be applied here. In the present computations, the grid cells have length 10 km. As shown in Figure 4, the Rossby radius $R^{(1)}$ for the first internal mode is nearly $2\Delta x$, whereas the Rossby radius $R^{(4)}$ for the fourth internal mode is approximately $0.5\Delta x$. According to an analysis of dispersion relations (e.g., [5], [14]), the C-grid gives a reasonably good approximation to the propagation of inertia-gravity waves if the Rossby radius exceeds Δx. However, if the Rossby radius equals $0.5\Delta x$, then the C-grid yields group velocity zero at all wavenumbers, in the case where all quantities are independent of y and the time integration is performed exactly. For smaller values of Rossby radius, the group velocity can have the wrong sign, so that energy propagates in the wrong direction.

On the other hand, the analysis of DG methods given in [14] indicates high accuracy for all wavenumbers, regardless of the relation between Rossby radius and grid size. In particular, see Figures 3-6 in [14], which show plots of dispersion
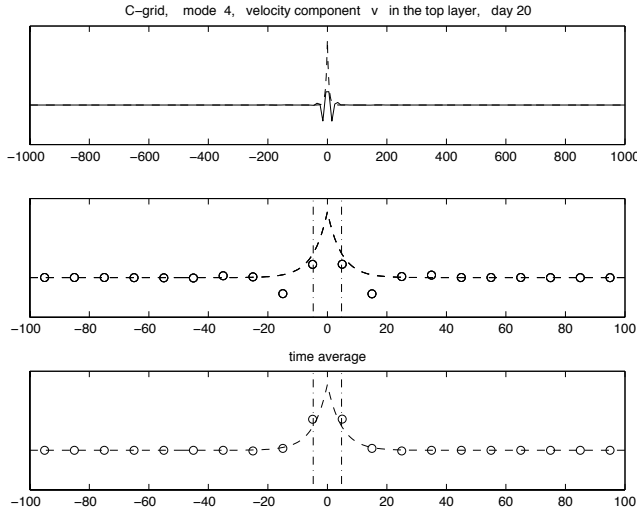
37

Figure 10: Values of v for the fourth internal mode, as computed with a C-grid code. At the model time shown here, very little adjustment has taken place, as the group velocity for inertia-gravity waves in this mode is nearly zero on a C-grid, with the present choice of parameters.

relations for $0 \leq k\Delta x \leq \pi$, where k is the wavenumber. Those plots include the cases $R = 2\Delta x$ and $R = 0.5\Delta x$, for both the continuous-time and discrete-time problems. In each plot, the physical mode in the dispersion relation for the DG method nearly coincides with the exact dispersion relation for inertia-gravity waves over the entire interval $0 \leq k\Delta x \leq \pi$.

6.4. Discussion of modes and efficiency

Some potential disadvantages of DG methods, relative to finite difference methods, is that they require the computation of multiple degrees of freedom per dependent variable in each grid cell at each time level, and for explicit time-stepping methods the stability constraints on the maximum allowable Courant number are more restrictive.

However, in some numerical experiments with shallow-water inertia-gravity waves reported in [14], the higher spatial accuracy of the DG methods compensated for those potential disadvantages. More specifically, for a given choice of Δx, solutions with finite difference methods on a B-grid and on a C-grid were computed with a much longer time step than could be used for a DG method. (With a B-grid, the values of velocity components are defined at the corners of mass cells.) However, the B-grid and C-grid solutions were much less accurate than the DG solution. Major reductions in Δx, and thus Δt, produced finite-difference solutions with accuracy comparable to the DG solutions, but those reductions eliminated the apparent advantages of the finite difference methods regarding Courant number and degrees of freedom.

For the case of the multi-layer geostrophic adjustment problem considered in the present paper, suppose that some number of internal modes needs to be modeled accurately. If a finite difference method based on the C-grid is used, then the grid size should be smaller than all of the corresponding Rossby radii. In contrast, a DG method does not require such a restriction, so a DG method can proceed with a substantially larger value of Δx than can be used with a C-grid code. This offsets (at least partially) the nominal disadvantages of DG methods associated with a restricted Courant number and the multiple degrees of freedom. A more precise comparison of efficiency depends on the number of internal modes that would need to be resolved.

The preceding remarks apply to the case of one horizontal dimension, where finite difference methods and DG methods are equally applicable. However, DG methods have significant advantages regarding applicability to unstructured meshes and irregular domains; those issues are beyond the scope of the present paper.

6.5. External mode

Finally, consider the case of the external mode, which corresponds to $j = 0$. The computations shown here for this mode have the same format as for the internal modes discussed above, except for two differences. First, as noted in Section 6.1, external waves move much more rapidly than internal waves, so for the plots shown in the present case the spatial interval is longer and the time intervals are shorter. Second, the parameter ϵ in the initial condition (A.30) is taken to be $\epsilon = 0.001$. This quantity represents the maximum relative perturbation in layer thicknesses at the initial time. In the case of an external mode, all layers are thickened or thinned by approximately the same proportion, at each time and horizontal location; over the 1000-meter depth of the fluid used in the present example, the value $\epsilon = 0.001$ produces a perturbation of 1 meter in the elevation of the free surface.

Figure 11 shows a side view of the top 120 meters of the fluid. The solid curves show the positions of the free surface and the top three layer interfaces after 20 baroclinic time steps, i.e., after 320 minutes, as computed with the DG code. The dashed curves show the positions of those surfaces in the exact geostrophically-balanced steady state. The vertical dashed lines are located at $x = \pm R^{(0)}$, where $R^{(0)}$ is the Rossby radius of deformation for the external mode. As time increases, the discontinuities in the surfaces move out of the picture, and for large times the computed positions of the free surface and the interfaces essentially coincide with their positions in the geostropically-balanced steady state.

Figure 12 shows the velocity component v. A dashed curve shows the values of v in the geostropically-balanced steady state, and a solid curve shows v as computed with the DG code. As in the case of internal modes, the solution oscillates in time with angular frequency approximately equal to the Coriolis parameter f, with an amplitude that decays slowly in time. The solid curve shows a time average of v over 65 baroclinic time steps (which approximates one inertial period $2\pi/f$), beginning at baroclinic step 100 (1600 minutes). For

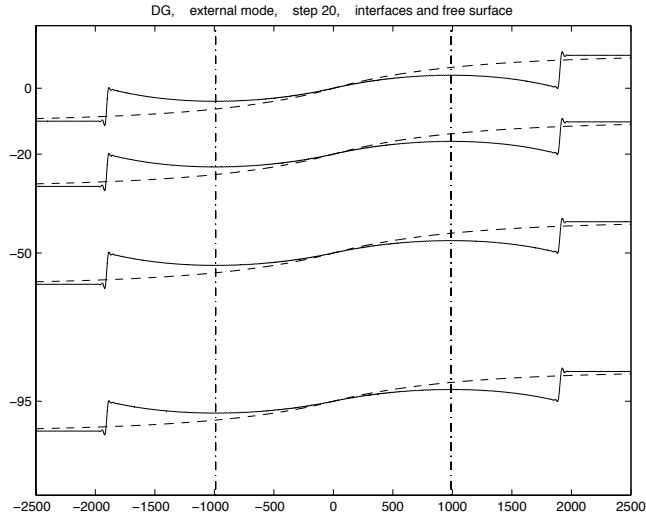DG,   external mode,   step 20,   interfaces and free surface

Figure 11: Side view of the top 120 meters of the fluid, for the external mode ($j = 0$). The solid curves show the free surface and the top three interfaces after 20 baroclinic time steps (320 minutes), as computed with the DG code, and the dashed curves show the positions of those surfaces in the geostrophically-balanced steady state. The vertical dashed lines are located at $x = \pm R^{(0)}$, where $R^{(0)}$ is the Rossby radius for this mode. In this plot, the perturbations from the rest states are multiplied by 10 for the sake of visibility.

the parameter value $\epsilon = 0.001$ used for the present computation, the maximum value of v in the steady-state solution is approximately 9.9 cm/sec. The two curves in the figure agree closely. Again, the DG code provides an accurate simulation of geostrophic adjustment.
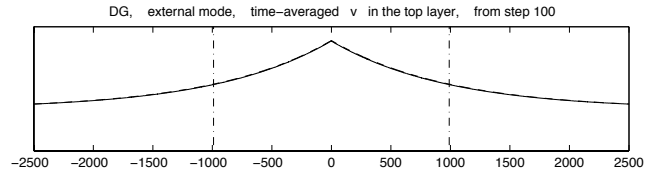

DG,   external mode,   time–averaged v in the top layer,   from step 100

Figure 12: Values of v for the external mode, as computed with the DG code. A solid curve shows the time average of v over one inertial period, beginning after 100 baroclinic time steps, and a dashed curve shows the values of v in the geostrophically-balanced steady state.

An accurate steady state for the external mode is also obtained in a computation with the C-grid code (not shown here). This is to be expected, as the Rossby radius of deformation for this mode is much greater than the grid size, and in this case the C-grid gives better representations of inertia-gravity waves than it does when the Rossby radius is comparable to or smaller than the grid size. However, the C-grid computation for the present problem shows sub-

stantial numerical dispersion near the location of the propagating discontinuity, whereas this effect is much less pronounced in the DG solution.

7. Summary

This paper discusses three issues related to the usage of discontinuous Galerkin methods for the numerical solution of multi-layer models of ocean circulation.

(1) The weak form of the pressure forcing that is developed here includes a vertical integral of the pressure. At a cell edge this is problematic, since the pressure in a DG formulation may be discontinuous across cell edges. In principle, values of the solution at a cell edge can be obtained by solving a Riemann problem for the full system, but in a multi-layer model with many layers this process could be complicated.

Instead, a simpler formulation can be obtained by using the idea of barotropic-baroclinic splitting to confine the Riemann problem to a simpler system of lower spatial dimension. In this formulation, a Riemann problem for the barotropic equations yields a free surface that is continuous at a cell edge. When this is combined with the baroclinic solution, the internal interfaces between layers can be discontinuous across the cell edge. However, in such a state any discontinuities in pressure across the cell edge are small, due to the continuity of the free surface and the small vertical variations in the density of the fluid. The pressure at the cell edge is then obtained via a simple average of left and right limits.

(2) For a barotropic-baroclinic time splitting in an ocean circulation model, a widely-used procedure is to (i) solve the governing equations in each layer explicitly with a relatively long time step, and (ii) solve the vertically-integrated barotropic equations either explicitly with a relatively short time step or implicitly with a long step. Explicit solutions of the barotropic equations are considered here. At the end of each long time step, the numerical solutions of the layer equations must be adjusted so that the vertical sums of the layer variables are equal to the corresponding variables computed with the barotropic equations. Any inconsistencies between the layer equations and the barotropic equations are at the level of truncation error, and the enforcement of consistency amounts to a manipulation of truncation error.

In the case of a DG formulation, the condition of consistency is expressed in terms of the degrees of freedom for the dependent variables. For the formulation that is developed here, the adjustments of the layer variables are obtained via correction terms that amount to subtracting the unresolved fast part of the forcing from the layer equations and then replacing this part with the time average of well-resolved forcing that is computed when the barotropic equations are solved explicitly with short time steps. This process is a kind of time filtering of the forcing terms, and it appears to be a mechanism that enables the layer equations to be solved stably with a long time step.

(3) The ideas described above are tested in a model problem involving geostrophic adjustment in a multi-layer fluid. During such an adjustment, a fluid that is not in geostrophic balance adjusts to a balanced state via propagation of waves away from the location of the imbalance. For the multi-layer

example described in this paper, the adjustment takes place via internal and/or external inertia-gravity waves. Explicit representations of the balanced state are derived here analytically.

With the barotropic-baroclinic splitting used here, the internal motions are modeled almost entirely by the baroclinic equations (i.e., the layer equations with the time filtering of forcing implied by the adjustments described above), and the external motions are modeled almost entirely by the vertically-integrated barotropic equations. The usage of external and internal modes then makes it possible to test the barotropic and baroclinic subsystems independently. In the tests described here, the DG representations for each subsystem provide accurate simulations of geostrophic adjustment for their respective modes.

References

[1] V. Aizinger, C. Dawson, The local discontinuous Galerkin method for three-dimensional shallow water flow, Comput. Methods Appl. Mech. Engrg. 196 (2007) 734–746.

[2] L. Bao, R.D. Nair, H.M. Tufo, A mass and momentum flux-form high-order discontinuous Galerkin shallow water model on the cubed-sphere, J. Comput. Phys. 271 (2014) 224–243.

[3] R. Bleck, L.T. Smith, A wind-driven isopycnic coordinate model of the north and equatorial Atlantic Ocean 1. Model development and supporting experiments, J. Geophysical Research 95C (1990) 3273–3285.

[4] C. Dawson, C.J. Trahan, E.J. Kubatko, J.J. Westerink, A parallel local timestepping Runge-Kutta discontinuous Galerkin method with applications to coastal ocean modeling, Comput. Methods Appl. Mech. Engrg. 259 (2013) 154–165.

[5] J.K. Dukowicz, Mesh effects for Rossby waves, J. Comput. Phys. 119 (1995) 188–194.

[6] A.E. Gill, Atmosphere-Ocean Dynamics, Academic Press, San Diego, 1982.

[7] F.X. Giraldo, T. Warburton, A high-order triangular discontinuous Galerkin oceanic shallow water model, Int. J. Numer. Meth. Fluids 56 (2008) 899–925.

[8] S. Gottlieb, D.I. Ketcheson, C.W. Shu, High order strong stability preserving time discretizations, J. Sci. Comput. 38 (2009) 251–289.

[9] S.M. Griffies, Fundamentals of Ocean Climate Models, Princeton University Press, Princeton, N.J., 2004.

[10] R.L. Higdon, A two-level time-stepping method for layered ocean circulation models: further development and testing, J. Comput. Phys. 206 (2005) 463–504.

[11] R.L. Higdon, Numerical modelling of ocean circulation, Acta Numerica 15 (2006) 385–470.

[12] R.L. Higdon, A comparison of two formulations of barotropic-baroclinic splitting for layered models of ocean circulation, Ocean Modelling 24 (2008) 29–45.

[13] R.L. Higdon, Physical and computational issues in the numerical modeling of ocean circulation, in: C. Dawson, M. Gerritsen (Eds.), Computational Challenges in the Geosciences, Springer, New York, 2013, pp. 1–23.

[14] R.L. Higdon, Pressure forcing and dispersion analysis for discontinuous Galerkin approximations to oceanic fluid flows, J. Comput. Phys. 249 (2013) 36–66.

[15] T. Kärnä, V. Legat, E. Deleersnijder, A baroclinic discontinuous Galerkin finite element model for coastal flows, Ocean Modelling 61 (2013) 1–20.

[16] M.A. Kopera, F.X. Giraldo, Analysis of adaptive mesh refinement for IMEX discontinuous Galerkin solutions of the compressible Euler equations with application to atmospheric simulations, J. Comput. Phys. 275 (2014) 92–117.

[17] E.J. Kubatko, J.J. Westerink, C. Dawson, hp discontinuous Galerkin methods for advection dominated problems in shallow water flow, Comput. Methods Appl. Mech. Engrg. 196 (2006) 437–451.

[18] E.J. Kubatko, B.A. Yeager, D.I. Ketcheson, Optimal strong-stability-preserving Runge-Kutta time discretizations for discontinuous Galerkin methods, J. Sci. Comput. 60 (2014) 313–344.

[19] R.J. LeVeque, Finite Volume Methods for Hyperbolic Problems, Cambridge University Press, Cambridge, UK, 2002.

[20] R.D. Nair, H.W. Choi, H.M. Tufo, Computational aspects of a scalable high-order discontinuous Galerkin atmospheric dynamical core, Computers and Fluids 38 (2009) 309–319.

[21] M.R. Petersen, D.W. Jacobsen, T.D. Ringler, M.W. Hecht, M.E. Maltrud, Evaluation of the arbitrary Lagrangian-Eulerian vertical coordinate method in the MPAS-Ocean model, Ocean Modelling 86 (2015) 93–113.

[22] T. Ringler, M. Petersen, R.L. Higdon, D. Jacobsen, P.W. Jones, M. Maltrud, A multi-resolution approach to global ocean modeling, Ocean Modelling 69 (2013) 211–232.

[23] B. Seny, J. Lambrechts, T. Toulorge, V. Legat, J.F. Remacle, An efficient parallel implementation of explicit multirate Runge-Kutta schemes for discontinuous Galerkin computations, J. Comput. Phys. 256 (2014) 135–160.

[24] D. Wirasaet, E.J. Kubatko, C.E. Michoski, S. Tanaka, J.J. Westerink, C. Dawson, Discontinuous Galerkin methods with nodal and hybrid modal/nodal triangular, quadrilateral, and polygonal elements for nonlinear shallow water flow, Comput. Methods Appl. Mech. Engrg. 270 (2014) 113–149.

Appendix A. Geostrophic adjustment in a multi-layer fluid

Here we develop exact steady-state solutions for the geostrophic adjustment problem that is used in the numerical computations described in Section 6.

Appendix A.1. Governing equations

Assume that the fluid consists of a stack of layers having constant specific volumes $\alpha_1 > \alpha_2 > \ldots > \alpha_L$, with indices increasing downward. In this special case, the lateral pressure forcing in each layer can be expressed as ∇M, where $\nabla = (\partial/\partial x, \partial/\partial y)$, and $M = \alpha p + gz$ is the Montgomery potential. (See, e.g., [11].) The hydrostatic condition $\partial p/\partial z = -\rho g = -g/\alpha$ implies $\partial M/\partial z = 0$ within a layer of constant density. In the case of a single-layer fluid, $\nabla M = \nabla(\alpha p_{top} + gz_{top})$; if the atmospheric pressure p_{top} is constant, then $\nabla M = g\nabla z_{top}$. This latter quantity is the pressure forcing term for the shallow water equations, so the Montgomery potential provides a generalization of the shallow-water forcing to the multi-layer case.

Now assume that the flow is a small perturbation of the rest state consisting of zero velocity and a level free surface and level interfaces between layers, and also assume that the bottom of the fluid domain is level. Denote the equilibrium pressures at the free surface and interfaces by $\tilde{p}_0$, $\tilde{p}_1$, ..., $\tilde{p}_L$; here, $\tilde{p}_r$ refers to the bottom of layer r if $1 \leq r \leq L$. Also let $\Delta\tilde{p}_r = \tilde{p}_r - \tilde{p}_{r-1} > 0$ denote the vertical pressure increment across layer r in the rest state. Denote the perturbations in pressures at the free surface and interfaces by $p_0 = 0$, $p_1(x,t)$, ..., $p_L(x,t)$; the quantity $\Delta p_r(x,t) = p_r(x,t) - p_{r-1}(x,t)$ is then the perturbation in the vertical pressure increment across layer r. (This notation differs from the notation introduced in Section 2, where p_r and Δp_r refer to total values instead of perturbations.) Also let $\tilde{M}_r$ denote the Montgomery potential in layer r at the rest state, and let M_r denote the perturbation in Montgomery potential in that layer.

As initially assumed in Section 2.2, assume here that all flow variables are independent of y and that the Coriolis parameter f is nonzero and constant. In this setting, the linearized governing equations can be written as

$$\frac{\partial u_r}{\partial t} - fv_r = -\frac{\partial M_r}{\partial x} \tag{A.1}$$

$$\frac{\partial v_r}{\partial t} + fu_r = 0 \tag{A.2}$$

$$\frac{\partial}{\partial t}(\Delta p_r) + (\Delta\tilde{p}_r)\frac{\partial u_r}{\partial x} = 0 \tag{A.3}$$

for $1 \leq r \leq L$, and

$$M_r - M_{r+1} = p_r(\alpha_r - \alpha_{r+1}) \tag{A.4}$$

for $1 \leq r \leq L - 1$. Equations (A.1)–(A.3) refer to fluid layer r. Equation (A.4) applies to interface r, which lies at the bottom of layer r and thus separates layers r and $r + 1$. This interface condition follows from the fact that α jumps across an interface, whereas z does not.

A boundary condition at the top of the fluid can be obtained from the fact that the pressure perturbation p_0 satisfies $p_0 = 0$, since the rest state and the perturbed states experience the same atmospheric pressure. At the bottom of the fluid, the perturbation in Montgomery potential satisfies

$$M_L(x,t) = \alpha_L p_L(x,t), \tag{A.5}$$

since there can be a nonzero perturbation in bottom pressure but not in bottom elevation.

The system (A.1)–(A.4) can be reduced to three equations by using the algebraic relation (A.4) to eliminate the variable Δp_r from the mass equation (A.3); the resulting system then consists entirely of differential equations. For simplicity, assume that $\alpha_1, \ldots, \alpha_L$ are evenly spaced with increment $\Delta\alpha > 0$. At each interior interface (i.e., $1 \leq r \leq L - 1$), $p_r = (M_r - M_{r+1})/\Delta\alpha$. Therefore, for the interior layers (i.e., $2 \leq r \leq L - 1$),

$$\begin{aligned}
\Delta p_r \;=\; p_r - p_{r-1} \;&=\; \frac{M_r - M_{r+1}}{\Delta\alpha} - \frac{M_{r-1} - M_r}{\Delta\alpha} \\
&=\; \frac{-M_{r-1} + 2M_r - M_{r+1}}{\Delta\alpha}.
\end{aligned} \tag{A.6}$$

For the top layer ($r = 1$), the upper boundary condition $p_0 = 0$ implies

$$\Delta p_1 \;=\; p_1 - p_0 \;=\; p_1 \;=\; \frac{M_1 - M_2}{\Delta\alpha}. \tag{A.7}$$

In the case of the bottom layer ($r = L$), the boundary condition (A.5) implies

$$\begin{aligned}
\Delta p_L \;&=\; p_L - p_{L-1} \\
&=\; \frac{M_L}{\alpha_L} - \frac{M_{L-1} - M_L}{\Delta\alpha} \\
&=\; \frac{1}{\Delta\alpha}\left[\left(1 + \frac{\Delta\alpha}{\alpha_L}\right)M_L - M_{L-1}\right].
\end{aligned} \tag{A.8}$$

Equations (A.6)–(A.8) can be combined into the form

$$\Delta p_r \;=\; \frac{(DM)_r}{\Delta\alpha} \tag{A.9}$$

for $1 \leq r \leq L$, where the definition of $(DM)_r$ is inferred from (A.6)–(A.8), and the result can be inserted into (A.3) to obtain

$$\frac{\partial}{\partial t}\left((DM)_r\right) + (\Delta\alpha)(\Delta\tilde{p}_r)\frac{\partial u_r}{\partial x} \;=\; 0. \tag{A.10}$$

The resulting system (A.1), (A.2), (A.10) has unknowns u_r, v_r, M_r for $1 \leq r \leq L$.

Appendix A.2. Modal solutions

The unknowns u_r, v_r, M_r are all associated with layers, not interfaces. Here, we obtain modal (separated) solutions in which these unknowns have the same vertical dependences. When functions of the form

$$
\begin{aligned}
u_r(x,t) &= \hat{u}(x,t)\phi_r \\
v_r(x,t) &= \hat{v}(x,t)\phi_r \\
M_r(x,t) &= \hat{M}(x,t)\phi_r
\end{aligned}
\tag{A.11}
$$

are substituted into (A.1), (A.2), and (A.10), the result is

$$
\frac{\partial \hat{u}}{\partial t} - f\hat{v} = -\frac{\partial \hat{M}}{\partial x}
\tag{A.12}
$$

$$
\frac{\partial \hat{v}}{\partial t} + f\hat{u} = 0
\tag{A.13}
$$

for all (x,t) and

$$
(D\phi)_r \frac{\partial \hat{M}}{\partial t} + (\Delta\alpha)(\Delta\tilde{p}_r)\phi_r \frac{\partial \hat{u}}{\partial x} = 0
\tag{A.14}
$$

for $1 \leq r \leq L$ and all (x,t). Here, $(D\phi)_r$ has the same form as $(DM)_r$, but with the symbol ϕ replacing the symbol M. More precisely,

$$
\begin{aligned}
(D\phi)_1 &= \phi_1 - \phi_2 \\
(D\phi)_r &= -\phi_{r-1} + 2\phi_r - \phi_{r+1} \qquad \text{if } 2 \leq r \leq L-1 \\
(D\phi)_L &= -\phi_{L-1} + \left(1 + \frac{\Delta\alpha}{\alpha_L}\right)\phi_L.
\end{aligned}
\tag{A.15}
$$

Since equation (A.14) holds for all (x,t) and all r, there exists a constant μ such that

$$
(D\phi)_r = \mu(\Delta\alpha)(\Delta\tilde{p}_r)\phi_r = (\mu c^2)\frac{\Delta\alpha}{\alpha_L}\frac{\Delta\tilde{p}_r}{\tilde{p}_L}\phi_r
\tag{A.16}
$$

for $1 \leq r \leq L$, where $c = \sqrt{\alpha_L \tilde{p}_L}$. In the special case of a single layer of constant density, the hydrostatic condition implies $c = \sqrt{gh}$, where h is the thickness of the fluid layer; in that case c is the speed of gravity waves in the nondispersive limit.

The equations (A.16), for $1 \leq r \leq L$, can be written as a matrix eigenvalue problem

$$
A\phi = \lambda B\phi,
\tag{A.17}
$$

where ϕ is a column vector with components $\phi_1, \ldots, \phi_L$; A is an $L \times L$ tridiagonal matrix with entries implied by the equations in (A.15); $\lambda = \mu c^2$; and B is diagonal with diagonal entries implied by the right side of (A.16). The quantity $\lambda = \mu c^2$ is dimensionless. Standard arguments show that the eigenvalues λ of the problem (A.17) are real and positive; in addition, eigenvectors corresponding to distinct eigenvalues are orthogonal with respect to the inner product defined by the matrix B. Denote the eigenvalues of (A.17) by $\lambda^{(0)}, \lambda^{(1)}, \ldots, \lambda^{(L-1)}$, with

$0 < \lambda^{(0)} \le \lambda^{(1)} \le \ldots \le \lambda^{(L-1)}$, and let $\phi^{(0)}$, $\phi^{(1)}$, ..., $\phi^{(L-1)}$ be corresponding eigenvectors. These eigenvectors give the possible vertical dependences in the modal solutions (A.11).

Next consider the dependences with respect to (x, t) in those solutions. With the separation constant μ that is used in (A.16), the mass equation (A.14) can be written as

$$\mu \frac{\partial \hat{M}}{\partial t} \;+\; \frac{\partial \hat{u}}{\partial x} \;=\; 0. \tag{A.18}$$

For modal solutions of the form (A.11), the relations (A.9) and (A.16) imply

$$\Delta p_r(x, t) \;=\; \frac{(D\phi)_r}{\Delta \alpha} \hat{M}(x, t) \;=\; \mu (\Delta \tilde{p}_r) \phi_r \hat{M}(x, t);$$

thus

$$\frac{\Delta p_r(x, t)}{\Delta \tilde{p}_r} \;=\; \mu \hat{M}(x, t) \phi_r.$$

The quantity $\Delta p_r(x, t)/\Delta \tilde{p}_r$ is the relative perturbation in layer thickness, and it will be denoted here by $\delta_r(x, t)$. For the modal solutions considered here, this relative perturbation has the representation

$$\delta_r(x, t) \;=\; \mu \hat{M}(x, t) \phi_r \;\equiv\; \hat{\delta}(x, t) \phi_r, \tag{A.19}$$

so the mass equation (A.18) can be written as

$$\frac{\partial \hat{\delta}}{\partial t} \;+\; \frac{\partial \hat{u}}{\partial x} \;=\; 0, \tag{A.20}$$

and the u-component (A.12) of the momentum equation becomes

$$\frac{\partial \hat{u}}{\partial t} - f\hat{v} \;=\; -\frac{1}{\mu} \frac{\partial \hat{\delta}}{\partial x}. \tag{A.21}$$

The relation $\lambda = \mu c^2$ implies $1/\mu = (c/\sqrt{\lambda})^2$, where λ is an eigenvalue of (A.17).

Let $\hat{u}^{(j)}(x, t)$, $\hat{v}^{(j)}(x, t)$, and $\hat{\delta}^{(j)}(x, t)$ be the dependent variables in the system (A.21), (A.13), (A.20) corresponding to eigenvalue $\lambda^{(j)}$ and eigenvector $\phi^{(j)}$ of the eigenvalue problem (A.17). These functions satisfy the system

$$\frac{\partial \hat{u}^{(j)}}{\partial t} - f\hat{v}^{(j)} \;=\; -\left(\frac{c}{\sqrt{\lambda^{(j)}}}\right)^2 \frac{\partial \hat{\delta}^{(j)}}{\partial x} \tag{A.22}$$

$$\frac{\partial \hat{v}^{(j)}}{\partial t} + f\hat{u}^{(j)} \;=\; 0 \tag{A.23}$$

$$\frac{\partial \hat{\delta}^{(j)}}{\partial t} \;+\; \frac{\partial \hat{u}^{(j)}}{\partial x} \;=\; 0. \tag{A.24}$$

This system has the structure of the linearized shallow water equations in the case where all quantities are independent of y. Solutions take the form of inertia-gravity waves (see, e.g., Section 6.2 of [14]), and an analysis of the dispersion relations for such waves (with space-time dependences of the form $\exp(ikx - i\omega t)$)

shows that the waves are dispersive and that the limit of the group and phase velocities as $k \to \infty$ is $c/\sqrt{\lambda^{(j)}}$. For a solution arising from a localized signal, the long-time behavior on any bounded spatial interval consists of slow variation in x and time oscillations with an angular frequency approximately equal to f, assuming that any energy is present at such wavelengths. Examples are seen in Section 6.

In summary, for modal solutions of the form (A.11), the vertical dependences are given by the components of the eigenvectors $\phi^{(0)}$, $\phi^{(1)}$, ..., $\phi^{(L-1)}$, and the corresponding dependences with respect to (x, t) are given by solutions of the system (A.22)–(A.24). Arbitrary initial conditions can be satisfied via superposition. As illustrated by the example considered in Section 6, mode $j = 0$ is the external mode, and modes $j = 1$ through $j = L - 1$ are the internal modes.

Appendix A.3. Geostrophic adjustment in a model problem

We now derive exact steady-state solutions of the system (A.22)–(A.24) corresponding to a case of piecewise constant initial data. Combining these solutions with the vertical dependences given by the eigenvectors then produces steady-state solutions to the linearized governing equations for the multi-layer fluid. This case is a multi-layer analogue of a model problem for the linearized single-layer shallow water equations analyzed in the text by Gill [6]. The steady-state solutions are in geostrophic balance, and the transition from the initial state to the balanced state is an example of geostrophic adjustment. In this development, the external mode and the various internal modes are treated individually.

In the following discussion, the superscripts (j) are deleted from all quantities, for the sake of notational simplicity, but throughout it is understood that we are considering a single modal solution of the form (A.11).

It will be seen below that steady-state solutions of the system (A.22)–(A.24) depend on the initial state, and the determination of the final steady state is governed by the conservation of potential vorticity. For the case where all quantities are independent of y, the vorticity is $\zeta = \partial v/\partial x - \partial u/\partial y = \partial v/\partial x$. For a modal solution, the vorticity in layer r is

$$\zeta_r = \frac{\partial \hat{v}}{\partial x}\phi_r \equiv \hat{\zeta}(x, t)\phi_r.$$

Differentiate the v-equation (A.23) with respect to x and use the mass equation (A.24) to obtain

$$\frac{\partial}{\partial t}\left(\hat{\zeta} - f\hat{\delta}\right) = 0$$

and thus

$$\hat{\zeta}(x, t) - f\hat{\delta}(x, t) = \hat{\zeta}(x, 0) - f\hat{\delta}(x, 0) \tag{A.25}$$

for all (x, t). Equation (A.25) is a statement of the conservation of potential vorticity in the present setting.

To obtain steady-state solutions, delete the time derivatives in the system (A.22)–(A.24). The second and third equations then state $\hat{u} = 0$. The first equation becomes a statement of geostrophic balance, and a differentiation of that equation with respect to x yields

$$f\hat{\zeta} = \left(\frac{c}{\sqrt{\lambda}}\right)^2 \frac{\partial^2 \hat{\delta}}{\partial x^2}. \tag{A.26}$$

Let

$$R = \frac{1}{f}\left(\frac{c}{\sqrt{\lambda}}\right); \tag{A.27}$$

this quantity is the Rossby radius of deformation corresponding to the speed $c/\sqrt{\lambda}$ for inertia-gravity waves in the nondispersive limit, for the modal solution being considered here. Now substitute (A.27) and (A.25) into (A.26) to obtain

$$R^2 \frac{\partial^2 \hat{\delta}}{\partial x^2} - \hat{\delta} = \frac{1}{f}\left[\hat{\zeta}(x,0) - f\hat{\delta}(x,0)\right]. \tag{A.28}$$

Given initial data and boundary conditions, equation (A.28) is used to determine the steady state for $\hat{\delta}$. The steady-state version of the u-equation (A.22) then yields

$$\hat{v} = fR^2 \frac{\partial \hat{\delta}}{\partial x} \tag{A.29}$$

as the steady state for $\hat{v}$.

Now consider the special case where the initial state is defined by $\hat{u}(x,0) = \hat{v}(x,0) = 0$ for all x and

$$\hat{\delta}(x,0) = \begin{cases} \epsilon & \text{for } x > 0 \\ -\epsilon & \text{for } x < 0; \end{cases}$$

here, ϵ is a dimensionless nonzero constant that can have either sign. According to equation (A.19), the relative perturbation in the thickness of layer r at time $t = 0$ is then

$$\frac{\Delta p_r(x,0)}{\Delta \tilde{p}_r} = \delta_r(x,0) = \hat{\delta}(x,0)\phi_r = \begin{cases} \epsilon\phi_r & \text{for } x > 0 \\ -\epsilon\phi_r & \text{for } x < 0. \end{cases} \tag{A.30}$$

In this case $\hat{\zeta}(x,0) = 0$, so the right side of equation (A.28) is $-\hat{\delta}(x,0)$. For solutions of that equation, impose the boundary condition that $\hat{\delta}$ is bounded as $x \to \pm\infty$. Some calculations show that the resulting solution of equation (A.28) is

$$\hat{\delta}_{steady}(x) = \epsilon \, \text{sign}(x)\left(1 - e^{-|x|/R}\right), \tag{A.31}$$

where $\text{sign}(x) = 1$ if $x > 0$ and $\text{sign}(x) = -1$ if $x < 0$. The steady state values of the components of velocity are

$$\hat{u}_{steady}(x) = 0 \tag{A.32}$$

$$\hat{v}_{steady}(x) = \epsilon f R e^{-|x|/R}; \tag{A.33}$$

the latter equation follows from (A.29) and (A.31).

Multiplication of (A.31)–(A.33) by ϕ_r, the rth component of the eigenvector ϕ, then gives the velocity components u_r and v_r and the relative perturbation in layer thickness, $\delta_r = \Delta p_r(x,t)/\Delta\tilde{p}_r$, for layer r in the steady-state geostrophically-balanced modal solution corresponding to the initial data considered here. Some plots of solutions for some examples are shown in Section 6.